Department of Physics and Measurement Technology

Final Thesis

Investigation of Symmetries of Phonons in 4H and 6H-SiC by Infrared Absorption and Raman Spectroscopy

Hina Ashraf

ISRN: LiTH-IFM-EX-- 05/1524--SE

Linköpings universitet

Institute of Technology
Linköping University

Department of Physics and Measurement Technology

Linköpings Universitet
SE-581 83 Linköping, Sweden

IFM Institutionen för Fysik och Mätteknik, Biologi och Kemi

Datum
Date 2005-11-16

Språk
Language

Svenska/Swedish
x Engelska/English

Rapporttyp
Report category

Licentiatavhandling
x Examensarbete
C-uppsats
D-uppsats
Övrig rapport

ISBN

ISRN
LITH-IFM-EX--05/1524—SE

Serietitel och serienummer
Title of series, numbering

ISSN

URL för elektronisk version

Titel
Title

Investigation of Symmetries of Phonons in 4H and 6H-SiC by Infrared Absorption and Raman Spectroscopy

Författare
Author *Hina Ashraf*

Sammanfattning
Abstract

The goal of the project work has been to study the symmetry of the phonons in 4H and 6H-SiC for different measuring geometries by using two experimental techniques, Raman and infrared absorption (IR) spectroscopy, and a theoretical model. The Raman spectra were measured in different scattering configurations in order to obtain experimental data for detailed investigation of the phonon symmetries.

The gross features of the spectra obtained in different geometries can be explained using general group-theoretical arguments. Using a lattice-dynamics model, we have also calculated the angular dependence of the phonon energies near the centre of the Brillouin zone, as well as the phonon displacements in some high-symmetry directions. The theoretical results are used to interpret the Raman lines in different configurations, and it was possible to estimate that if ionicity of the bonding of 12% is taken in the theoretical model for 4H-SiC, the splitting of the polar TO mode and the shift of the polar LO mode observed in our spectra are well reproduced theoretically. It was also observed that these polar modes have to be classified as longitudinal and transversal with respect to the direction of phonon wave vector, while the rest of the modes remain longitudinal or transversal with respect to the c-axis of the crystal. The Raman lines in the case of 4H SiC have been tentatively labelled with the irreducible representations of the point group of the crystal (C_{6v}).

Nyckelord
Keyword
Raman Spectroscopy, Silicon Carbide (SiC), IR absorption sprectroscopy, Phonon displacements, Lattice dynamic Model (LDM), Polar modes in crystals.

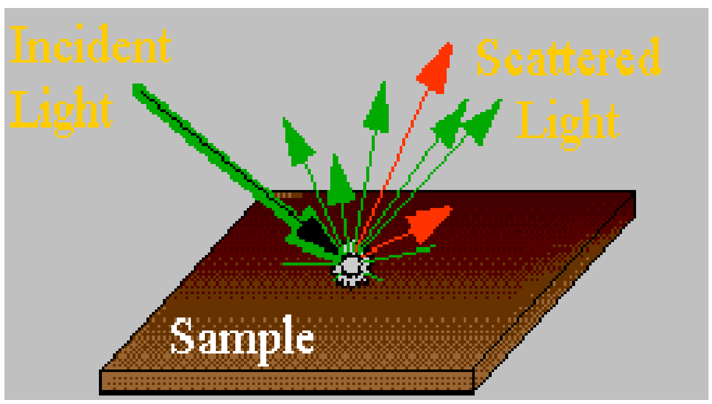

Investigation of Symmetries of Phonons in 4H and 6H-SiC by Infrared Absorption and Raman

Hina Ashraf

To my Parents…..

Cogito Ergo Sum
' I think, therefore I am'

Descartes

Abstract

The goal of the project work has been to study the symmetry of the phonons in 4H and 6H-SiC for different measuring geometries by using two experimental techniques, Raman and infrared absorption (IR) spectroscopy, and a theoretical model. The Raman spectra were measured in different scattering configurations in order to obtain experimental data for detailed investigation of the phonon symmetries.

The gross features of the spectra obtained in different geometries can be explained using general group-theoretical arguments. Using a lattice-dynamics model, we have also calculated the angular dependence of the phonon energies near the centre of the Brillouin zone, as well as the phonon displacements in some high-symmetry directions. The theoretical results are used to interpret the Raman lines in different configurations, and it was possible to estimate that if ionicity of the bonding of 12% is taken in the theoretical model for 4H-SiC, the splitting of the polar TO mode and the shift of the polar LO mode observed in our spectra are well reproduced theoretically. It was also observed that these polar modes have to be classified as longitudinal and transversal with respect to the direction of phonon wave vector, while the rest of the modes remain longitudinal or transversal with respect to the c-axis of the crystal. The Raman lines in the case of 4H SiC have been tentatively labelled with the irreducible representations of the point group of the crystal (C_{6v}).

Acknowledgement

I want to express my sincere gratitude to my supervisor Ivan Ivanov. His kind, informative and encouraging supervision were always with me during my theses period. He always gave me time and answered my questions with patience. His long discussions made it possible for me to understand and write this thesis.

I would like to thank Professor Eric Janzén, who gave me a very good opportunity to do my diploma work in material science group.

Many thanks go to Dr.Qamar for always encouraging me and always providing me moral support during my MS programme here at Linköping.

I also want to pay my gratitude to Prof. Leif Johansson, who always listened to the problems of students and is always very cooperative.

I would also like to thank my professors Dr. Raheel Ali and Dr.Khalid Khan, from Pakistan, who always encouraged me for looking forward and striving for more.

I also want to acknowledge my all classfellow of MS programme especially Amel, Shu Han, Garry, to my new friends with whom I got acquainted here, Harpreet, Sarita, Nosheen, Tahira Baji, Jawad, Kashif, and to my old friend Fawad. You were all continuous source of support for me. Because of all you, I enjoyed a lot during my stay here and never felt that i'm away from my family and home.

Finally I would like to acknowledge my family who always believed in me and my abilities and always appreciated me.

Contents

Motivation

Lattice Dynamic Models (LDM) usually predict the energies of phonons correctly but not the phonon displacements. We want to investigate to which extent the IR absorption and especially the Raman spectroscopy can be used to probe these atomic diplacements in 4H and 6H-SiC. Consequently, we need analysis of phonon symmetries for different scattering configurations measurements in IR and Raman.

The main goal of this diploma work is to label the Raman lines obtained experimentally by using theoretical arguments. The symmetry labels for these Raman lines, which correspond to phonon modes (in 4H and 6H-SiC in our case), used in literature are often very confusing and need justification.

Thus one of the main task was to collect a detailed experimental data (for Raman and IR of 4H and 6H-SiC), which will be used for much more detailed comparison with the theory (development in progress) in the future.

1. Silicon Carbide

1.1. Introduction

Silicon carbide is a ceramic compound of silicon (Si) and carbon (C), which was first observed in 1824 by Jöns Jacob Berzilius, a Swede. Silicon carbide (SiC) is also known as carborundum or moissanite. Natural SiC was found in meteorites and was discovered for the first time by Moissan in 1905. SiC is the only compound that exists in the Si-C system. The compound is hard and stable maintaining its mechanical properties at temperature above 1000^0C. It is the hardest and most resistant material after diamond. It has good thermal and chemical stability that make it resistant to corrosion.

SiC is known to be wide (indirect) band gap semiconductor and has also very fascinating and extraordinary electronic properties. The important electronic properties of SiC, which make it attractive for electronic devices, are high electron mobility, high breakdown field, high thermal conductivity and good radiation resistance. Due to its material properties, SiC is an excellent candidate for high temperature electronics. Device operation at higher temperatures than silicon (Si) and gallium arsenide (GaAs) based devices is possible. Systems utilizing SiC can operate with high current densities and require reduced external cooling. In addition, individual devices can operate at higher voltage reducing the number of components needed. This results in cost saving in high power systems. Some important device applications of SiC are sensor operating in ultraviolet region, nitride based LED's using SiC as substrate, cutting tools, RF and microwave devices such as base state transmitter or transmitter for digital TV, ultra fast Schottky diodes, used in air crafts and nuclear reactors, used as cutting tool, as substrate for GaN epitaxial growth etc.

The limitations of the SiC technology are due to defects characteristics for SiC, such as point defects, line defects or two dimensional plane defects. The most common defect in SiC is micropipes, which is very bad for the devices. Different methods have been employed to grow SiC. The growth can be divided into boule (bulk) growth and epitaxial growth. For boule growth the seeded sublimation growth method is widely used. Because of the phase equilibrium in the Si and C materials system (specifically, the material sublimes before it melts) the technique is based on Physical Vapor Transport (PVT). The technique is also called modified-Lely method or seeded sublimation growth and was invented in 1978 by Tairov et al [2]. It is used today for commercial fabrication of SiC wafers. Although the sublimation technique is relatively easy to implement, having in mind the high growth temperatures needed, the processes are difficult to control, particularly over large growth areas. Due to the low stacking fault energy it is difficult to restrict syntax (parasitic polytype formation) during bulk crystal growth and to grow a single polytype material. For example, 4H polytype falls within the same temperature range of occurrence as 6H polytype, while 3C can be formed over the whole temperature range used for SiC growth. Another alternative growth technique is High Temperature CVD (HTCVD) where transport of the growth species to the seed crystal is directly provided by high purity gas precursors containing Si- and C-species. The thermal environment and the growth rates achievable in this technique are to a large extent close to the PVT method.

Sublimation epitaxy has proven to be a suitable technique for growth of thick (up to 100 μm) epitaxial layers with smooth as-grown surfaces. Reproducible quality of these surfaces is obtained with growth rates ranging from 2 to 100 μm/h in the temperature range from 1600 to 1800°C. The structural quality of the epilayer improves compared to the substrate. The surface roughness is diminished in the sublimation epilayer. Another simple and elegant technique is Liquid phase epitaxy (LPE) with several advantages such as low process temperature, relatively high growth rate, easy for technical implementations in various geometries, doped layers and multiplayer structures. The main advantage, however, is that the process is carried out at relatively low temperature and close to thermodynamic equilibrium conditions, which presumes a low concentration of point defects in the epitaxial layers. Hence, the quality of the grown material is mainly limited by morphological features. LPE is particularly interesting for SiC because it has been found that micropipe closing takes place by this growth method. Micropipe closing for this technique was reported by Yakimova in 1995 [4].

1.2. Crystal Structure of SiC

SiC has strong bonding with a short bond length (1.89 Å) between a Si and C atom. The slight difference in electronegativity between these two atoms gives 12% ionicity to the otherwise covalent bonding, with the Si atom slightly positively charged. The basic building block of the crystal is a tetrahedron consisting of a C (Si) atom in the middle and four Si (C) atom at the four corners (fig .1.1).

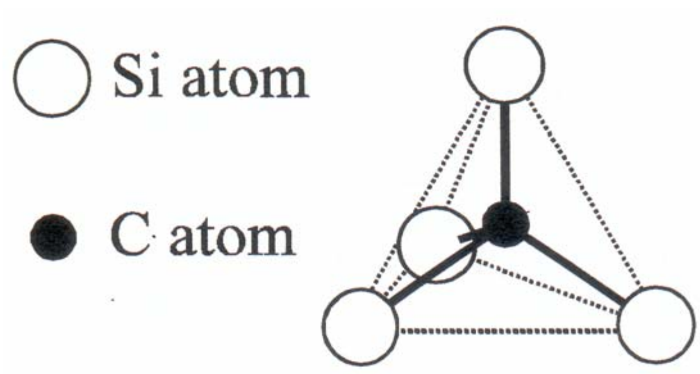

Fig.1.1. Si and C atoms arranged in a tetrahedron, which is smallest building block of crystal structure.

An important property of SiC is that it exhibits polytypism. Thus we can say that SiC is not a single semiconductor but a family of semiconductors. There are more than 200 polytypes of SiC and all but the simplest ones can be considered as natural superlattices. All SiC polytypes can be viewed as a stacking of close packed planes of double layers of Si and C atoms, as shown in fig.1.2.

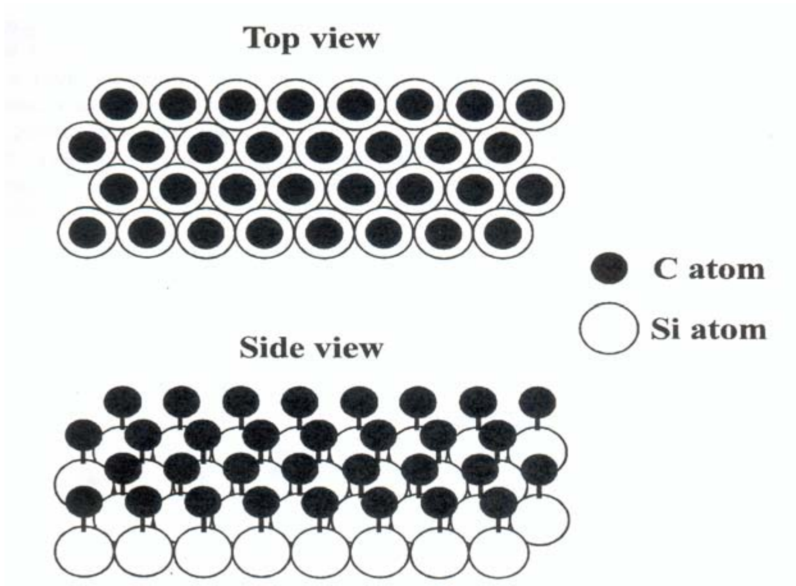

Fig.1.2. Arrangement of Si and C atoms in closed-packed double layer.

Different polytypes are formed by different stacking order of the close-packed double layers. Consider a single closed double layer of atoms on top of the first layer, the most stable configuration is formed if the atoms of the second layer are placed in the valleys of first layer. However there are two different possibilities to stack the second layer as depicted by fig. 1.3.

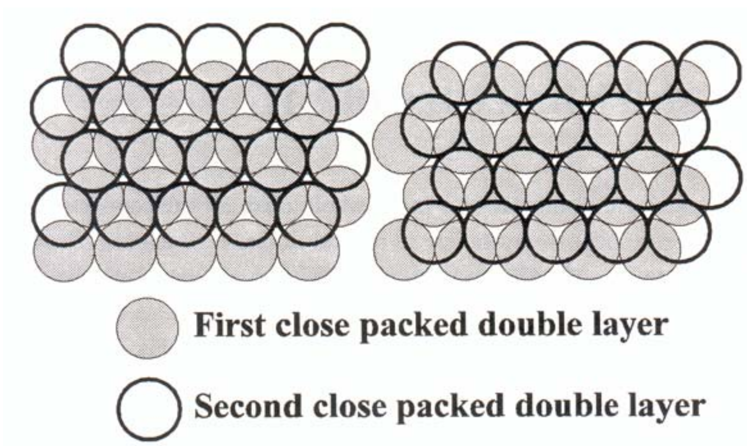

Fig.1.3. The second close-packed double layer can be placed in two different positions on top of the first close packed double layer.

The freedom to choose between two different positions of the second layer and by creating an ordering in the stacking sequence of the layers, gives rise to a variety of different polytypes. The stacking of double layers is most conveniently viewed in a

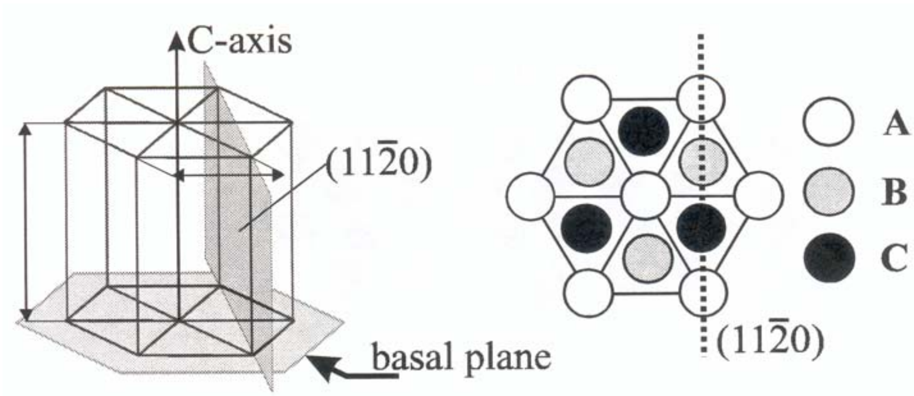

Fig.1.4. The hexagonal system to describe different polytypes and the three different positions, A, B, and C, respectively, of the double layers.

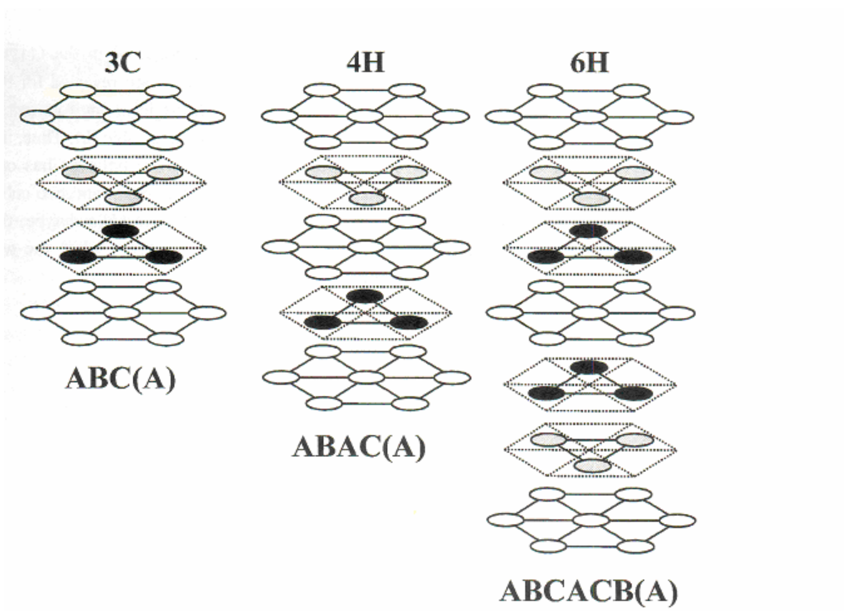

Fig.1.5. One stacking period of three common polytypes 3C, 4H and 6H-SiC

hexagonal system, as shown in fig.1.4, with three different position of the atom pair labeled A, B and C. The c-axis is perpendicular to the basal plane, which lies in the plane of the close packed double layer. The three most common and important polytypes of SiC are 3C, 4H and 6H, although 15R and 21R are also fairly common. Here the Ramsdell notation is used, where the number represent the number of bilayers per unit cell and the letter represents the type of Bravais lattice, i.e. H stands for hexagonal, C for cubic and R for rhombohedral. Consequently, there is no difference between the polytypes within the basal plane. It is the stacking sequence of double layers along the c- axis that gives rise to different polytypes.

If the stacking sequence of the different polytypes is projected in the $(11\bar{2}0)$ plane as indicated in fig. 1.6, we can observe difference in the local environment for different atomic sites. In the turning point the local environment is hexagonal (h) and between the the turning points, the local environment is cubic (k). 3C polytype has cubic structure since there is no turning point , the 4H polytype has one cubic and one hexagonal site (h,k) and the 6h polytype has one hexagonal and two cubic sites (h,k_1,k_2). For the cubic and the hexagonal lattice site in 4H and 6H polytypes, the arrangement of surrounding atoms differs from the second neighbours while the two cubic lattice sites k_1 and k_2 differ first in the third neighbours.

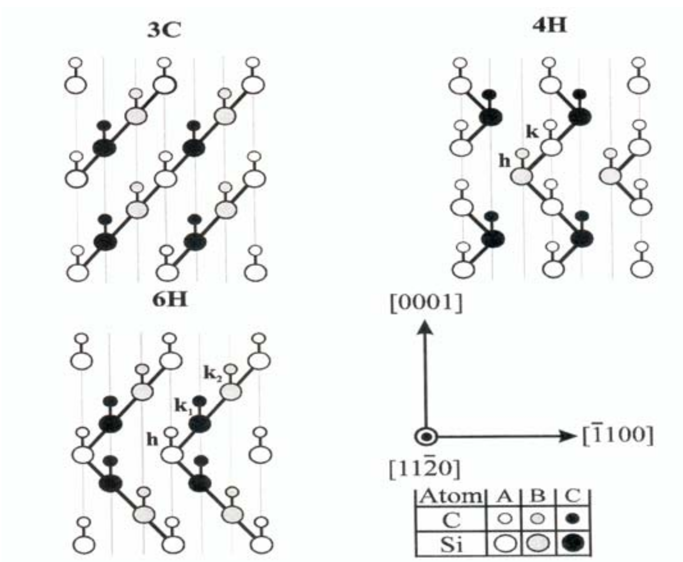

Fig.1.6. The ($11\bar{2}0$) plane of the three polytypes 3C, 4H and 6H.

2. Infrared Spectroscopy in Solids

Infrared spectroscopy is one of the most popular spectroscopic techniques in solid-state physics. The simple reason for this is that nearly all materials exhibit a more or less expressed structure of absorption in the IR spectral range. Absorption process due to transition across the energy gap, from excitons or from impurity states, is found in the visible spectral range as well as in the IR. Important additional sources for absorption and reflection are the IR active phonons or vibrational modes, which can give valuable supplementary information to results from Raman scattering. We will only be concerned with the absorption (and Raman scattering) due to the vibrational modes of crystal.

This chapter contains review of the principle of the Fourier transform infrared spectroscopy (FTIR), instrumentation, active phonon modes in IR energy range in solids and the classical theory of IR spectroscopy and IR bands in silicon carbide.

2.1. Basic Principle and Set-up for Fourier Spectroscopy.

Analysis in the Fourier spectroscopy is based on the absorption of IR light by the lattice-phonon modes. A Fourier spectrometer consists of Michelson interferometer, as shown in fig2.1. The white light from the source, which is a lamp, located at the focus of lens L_1 is separated into two beams of equal intensity by the beam splitter, which is half polished KBr mirror in our case. One of the beams is reflected from the mirror M_1 (fixed in position) and the other beam by the mirror M_2. Mirror M_2 is movable and can glide along its axis in a controllable way. After the beam splitter the two beams with different time delay (depending on the momentary position of M_2) will interfere and are focused on the detector after passing through the sample and a lens. The introduced time delay between beams reflected from mirror M_1 and M_2 would give different interference of beam for every position of mirror.

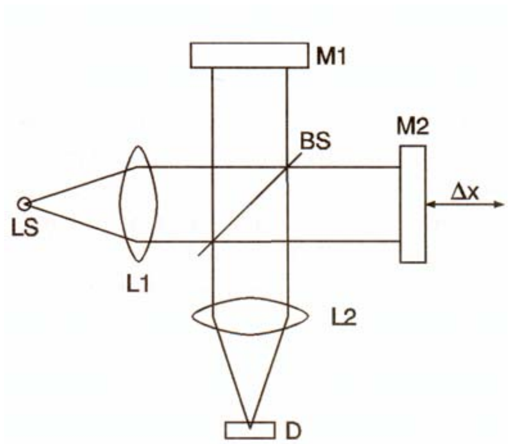

Fig. 2.1. Optical path in a Michelson Interferometer-; M: mirrors; BS: beam splitter; LS: light source; D: detector.

Hence the interferometer disperses the light in different wavelength by a totally different method as compared to prism. The light passing through the sample is then focused by the lens L_2 on the detector. The detector in our case was Deuterium Triglycine sulphate (DTGS). The electrical signal from the detector is amplified by a lock-in/analog to digital converter (ADC) system. The interferogram is registered on a recorder and Fourier transformed by a dedicated computer in order to obtain the spectral distribution of the received light.

It is always important to record two interferograms; one for the sample and another for a reference (i.e. a mirror) and later division of the background spectrum by the spectrum obtained with sample will give the desired spectrum. Fig.2.2 shows an example of the raw spectrum (sample plus background) together with the processed transmission spectrum for 6H- SiC.

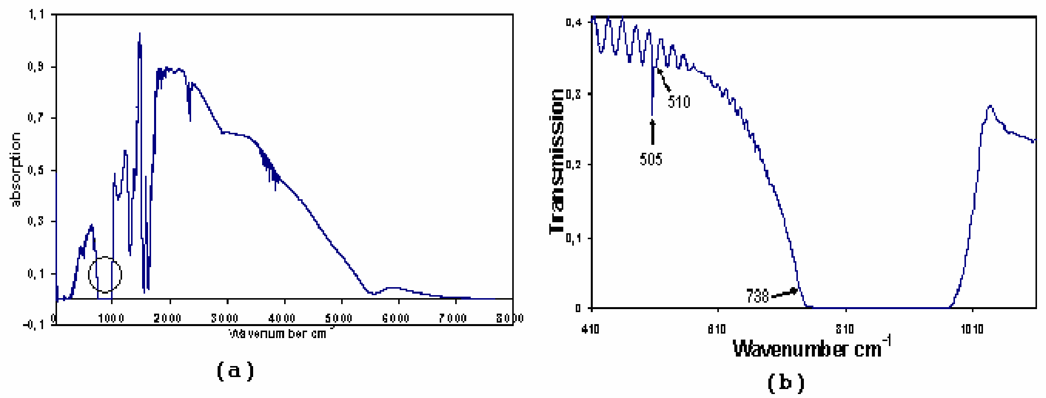

Fig. 2.2. a) The transmission spectrum for 6H-SiC with background. b) Transmission spectra after subtraction of background. The reference sample used was silver mirror. The region plotted in figure (b) is shown in fig(a) by a circle.

2.2. Infrared active phonons

As we know all atoms in solids hold in their equilibrium position by the forces that hold the crystal together. When atoms are displaced from their equilibrium positions, they experience restoring forces, and vibrate at characteristics frequencies (see fig 2.3a, 2.3b).

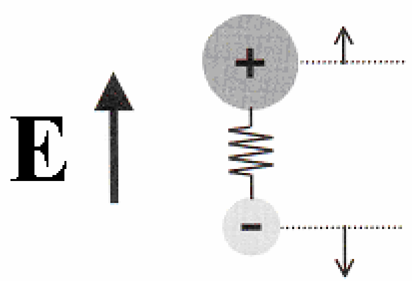

Fig.2.3a. Induced dipole moment in a solid as a result of interaction with the oscillating electric field (Classical Picture)

These vibrational frequencies are determined by the phonon modes of the crystal. The energies of the atomic vibrations are comparable to those of photons in the mid to far infrared range (typically 10-1000 cm^{-1}). Some of the vibrations are associated with the appearance of induced dipole moment (see fig.2.3a) and can interact directly with the electric field of incident light. They are called infrared active modes.

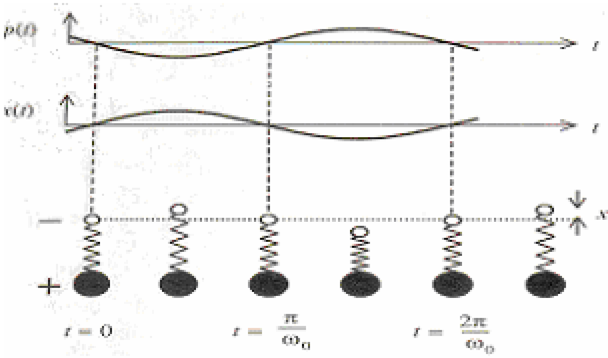

Fig2.3[b] **Oscillation of a classical dipole consisting of a heavy positive charge and a light negative charge bound together by a spring. X(t) is the time dependent displacement o f the negative charge from its equilibrium position. The natural vibrations of the dipole about the equilibrium position at frequency ω_0 generate a time dependant dipole moment p(t) as indicated in figure.**

Only optical phonons can be observed in IR spectrum and the reason behind this is that when photon of certain energy is absorbed with in a solid and a phonon is created, the conservation laws require that the photon and the phonon must have the same energy and momentum. This condition is only satisfied by optical modes.

We can explain this by the dispersion curves of optical and acoustic phonons in a simple crystal shown in fig2.4. The angular frequency ω of the optical and acoustic phonons is plotted against the wavevector k in the positive half of the first Brillouin zone (BZ). At small wave vectors the slope of the acoustic branch is equal to ν_{sound} in the medium, while the optical modes are dispersionless near k ≅0. The dispersion of light waves (shown by dotted line) in crystal has constant slope of $\nu = c/n$, where n is the refractive index. The requirement that the phonon and photon both should have same frequency and wave vector is satisfied when the dispersion curves intersect. Since $c/n >> \nu_{sound}$, the only intersection point for the acoustic branch occurs at the origin, which corresponds to the response of the crystal to a static electric field. For optical branch, intersection occurs at finite ω, which is shown in fig.2.4 by circle.

Electromagnetic waves are transverse and therefore couple more strongly with transverse optical modes of crystal. But we cannot neglect longitudinal optical (LO) modes as we will see later that they play important role in the infrared properties of crystals. Coupling of the phonon with the photon is due to the driving force exerted on crystal by the oscillating electric field of the wave. It can only happen when the crystal has polar character. The polar character of compound solid mainly depends on the nature of bonding. In covalent crystals with predominant covalent bonding, different size and charge of the constituting atoms will introduce polar character.

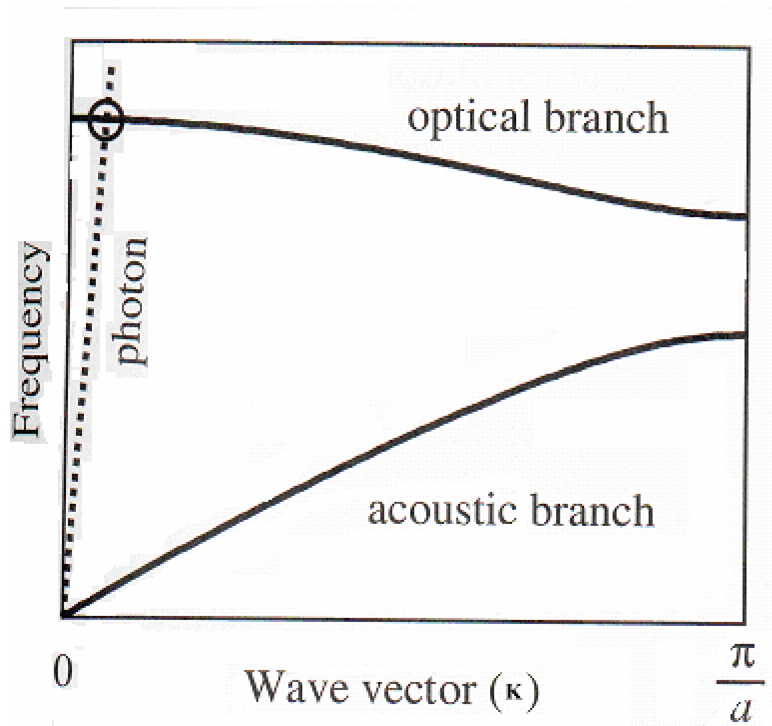

Fig. 2.4. Dispersion curves for the acoustic and optical phonon branches in a typical crystal with a lattice constant of a. the dispersion of photon is shown by dotted lines.

2.3. Classical theory of IR absorption and transmission.

The interaction between electromagnetic waves and transverse optical (TO) phonons can be treated by classical oscillator model. Consider a linear chain of unit cell, which consist of negative (grey) and positive (black) ions as shown in fig2.5. If the direction of propagation of the electromagnetic wave is along the z direction, then the displacement of atoms will be in x or y direction for the transverse modes. Furthermore, for optic modes the atoms will move in opposite directions with fixed ratio between their displacements.

As we are interested in TO phonons with k ≈ 0 and an infrared photon of the same frequency and wave number, this implies that we are considering phonons of very long wavelength ~ 10^{-4}cm^{-1} matched to that of an infrared photon. This wavelength is quite long when we compare it with the dimensions of a lattice. For such long wavelength, the behavior of propagation of TO modes within a crystal is almost identical.

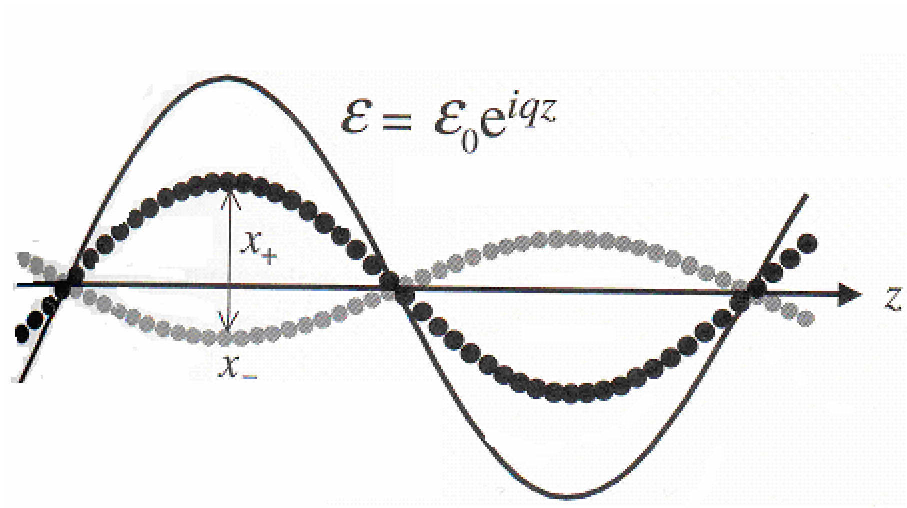

Fig.2.5. Interaction of a TO phonon mode propagating in the z direction with an electromagnetic wave of the same vector. The black circles represent positive ions, while the grey circles represent the negative ions. The solid line represents the spatial dependence of the electric field of the electromagnetic wave.

We can write equations of motion for the displacement of ions as a result of interaction of TO phonons with the oscillating electric field of the light waves.

$$m_+ \, d^2x/dt^2 = -C(x_+ - x_-)eE(t),$$

$$m_- \, d^2x/dt^2 = -C(x_- - x_+)eE(t), \quad \textbf{(2.1)}$$

where m_+ and m_- are the masses of two ions, C is the restoring constant of the medium, E(t) is the electric field due to the light wave and 'e' is the effective charge per ion and is taken as ±e.

After following simple arithmetic steps, eq 2.1 can be written as

$$d^2x / dt^2 + \varpi_{TO}^2 x = \frac{e}{\mu} E(t) \quad , \tag{2.2}$$

where

$\frac{1}{\mu} = \frac{1}{m_+} + \frac{1}{m_-}$, defines the reduced mass,

$x = x_+ - x_-$,

and

$$\varpi_{TO}^2 = \frac{C}{\mu}.$$

Eq.2.2 represents the undamped oscillation of the crystal lattice in response to the oscillating electric field of light but as the lattice modes or phonons have finite lifetimes we should introduce also a damping term γ in eq.2.2.

$$\frac{d^2x}{dt^2} + \gamma \frac{dx}{dt} + \omega_{TO}^2 x = \frac{e}{\mu} E(t) \tag{2.3}$$

Eq.2.3 now represents the response of a damped TO mode to resonant light wave.
Substitute $x(t) = x_0 \exp(-\iota\varpi t)$ and $E(t) = E_0 \exp(-\iota\varpi t)$ in eq.2.3. We get,

$$x_0 = -\frac{eE_0}{m(\varpi_{TO}^2 - \varpi^2 - \iota\gamma\varpi)} \, . \tag{2.4}$$

as a steady state amplitude of the forced oscillation.

The oscillation of ions within crystal will produce a time varying dipole moment p (t) = -e x(t) as shown in fig.2.3b. This gives a resonant contribution to the polarization of the medium. If N is the number of atoms per unit volume, the resonant polarization is given by

$$P_{resonant} = Np \, ,$$

$$P_{resonant} = -Nex = \frac{Ne^2 E}{m_0(\varpi_{TO}^2 - \varpi^2 - \iota\gamma\varpi)} \quad . \tag{2.5}$$

From eq.2.5, we can see that the resonant polarization has largest magnitude when ω is equal to ω_{TO}. This is also one of the properties of forced oscillations in classical mechanics.

The electric displacement D of the medium can be related to the to the electric field E and the polarization P through,

$$D = \varepsilon_0 E + P_{background} + P_{resonant} \, ,$$

$$D = \varepsilon_0 E + \varepsilon_0 \chi E + P_{resonant} \, . \tag{2.6}$$

where $P_{background}$ represents the non-resonant term and accounts for all the contribution to the background susceptibility χ of medium arising from the polarization due to all other oscillators at high frequency. To simplify the mathematics, we will assume that the material is isotropic so we can write,

$$D = \varepsilon_0 \varepsilon_r E \quad . \tag{2.7}$$

Combining eqs 2.5 – 2.7, we obtain,

$$\varepsilon_r(\varpi) = 1 + \chi + \frac{Ne^2}{\varepsilon_0 \mu(\varpi_{TO}^2 - \varpi^2 - \iota\gamma\varpi)} , \tag{2.8}$$

where ε_r (ω) is the complex dielectric constant at angular frequency ω. Eq 2.8 can be written in terms of static (ε_{st}) and high frequency (ε_∞) dielectric constant respectively. In the limits of low and high frequency, we obtain from eq 2.8,

$$\varepsilon_{st} \equiv \varepsilon_r(0) = 1 + \chi + \frac{Ne^2}{\varepsilon_0 \mu \omega_{TO}^2} , \tag{2.9}$$

$$\varepsilon_\infty \equiv \varepsilon_r(\infty) = 1 + \chi \, . \tag{2.10}$$

Thus eq. 2.8 can be written as

$$\varepsilon_r(\varpi) = \varepsilon_\infty + (\varepsilon_{st} - \varepsilon_\infty)\frac{\varpi_{TO}^2}{(\varpi_{TO}^2 - \omega^2 - \iota\gamma\omega)}, \tag{2.11}$$

where ε_∞ represents the dielectric function at frequencies well above the phonon resonance but below the next natural frequency of crystal due to (for example) the bound electronic transition in the visible/ultraviolet spectral region.

If we take the damping constant γ equal to zero at certain frequency ω′then we can write eq. 2.11 as

$$\varepsilon_r(\varpi') = 0 = \varepsilon_\infty + (\varepsilon_{st} - \varepsilon_\infty)\frac{\varpi_{TO}^2}{(\varpi_{TO}^2 - \omega'^2)}. \qquad \textbf{(2.12)}$$

Thus the dielectric constant can fall equal to zero

From eq.2.12 we find

$$\omega' = (\frac{\varepsilon_{st}}{\varepsilon_\infty})^{\frac{1}{2}}\varpi_{TO}. \qquad \textbf{(2.13)}$$

For a medium with no free charges, the total charge density is equal to zero and we can write

$$\nabla.D = \nabla.(\varepsilon_r\varepsilon_0 E) = 0$$

where

$$E(r,t) = E_0 \exp \iota(k.r - \varpi t)$$

If $\varepsilon_r \neq 0$, we can conclude that **k.E = 0** and this tells us that the electric field must be transversal (perpendicular to the direction of the wave) and, therefore, the coupling is strong between TO phonons and the transverse electric field of photon, but if we take
$\varepsilon_r = 0$, we can satisfy eq.2.13 with waves in which **k.E ≠ 0**, that is, longitudinal waves. Thus we conclude that the longitudinal electric field is present at frequencies for which $\varepsilon_r(\omega) = 0$. In the same way the TO phonon modes generate a transverse electric field wave, the LO phonon modes generate a longitudinal electric field wave. Thus the waves

at $\omega = \omega'$ correspond to LO phonon waves, and we identify ω' with the frequency of the LO mode at q = 0, namely, ω_{LO}.

This allows us to write eq 2.13 as

$$\frac{\varpi_{LO}^2}{\omega_{TO}^2} = \left(\frac{\varepsilon_{st}}{\varepsilon_{\infty}} \right) \quad \textbf{(2.14)}$$

This result is known as Lyddane-Sachs- Teller (LST) relation. The validity of the LST relation can be checked by comparing experimental values of $\frac{\omega_{LO}}{\omega_{TO}}$ for some experiment as Raman scattering with the one calculated from eq 2.14 using known values of the dielectric constant.

An interesting result form eq 2.14 is that when $\varepsilon_{st} = \varepsilon_{\infty}$, the LO and TO modes are degenerate. Hence we can say, $\varepsilon_{st} = \varepsilon_{\infty}$, when there is no infrared resonance which is the case for non-polar elementary crystals as Si, Ge etc.

2.4. IR Absorption coefficients

The Lattice absorbs very strongly whenever the photon is in resonance with the TO phonon. Actually the polar solids have such high absorption coefficients in the infrared region that, unless the crystal is less than 1μm thick, no light at all will be transmitted. It is important to have thin film samples to observe lattice absorption in this case.

We can calculate the absorption coefficient from eq.2.11, using the imaginary part of the dielectric function. From the relation given in eq.2.15,

$$\varepsilon_r(\varpi) = \varepsilon_1 + \iota\varepsilon_2 , \quad \textbf{(2.15)}$$

we obtain

$$k = \frac{(-\varepsilon_1 + (\varepsilon_1^2 + \varepsilon_2^2)^{\frac{1}{2}})^{\frac{1}{2}}}{\sqrt{2}} \quad , \tag{2.16}$$

where k is the extinction coefficient. The absorption coefficient α can be calculated from k using the relation given in eq.2.17,

$$\alpha = \frac{4\pi k}{\lambda} \; . \tag{2.17}$$

If we analyze eq.2.14 in more detail we can observe some important features.

For $\gamma = 0$, the eq.2.11 can again be written as

$$\varepsilon_r(\varpi') = \varepsilon_\infty + (\varepsilon_{st} - \varepsilon_\infty)\frac{\varpi_{TO}^2}{(\varpi_{TO}^2 - \omega'^2)} . \tag{2.18}$$

Lets consider concrete values, ν_{TO} = 10THz, ν_{LO} = 11THz, ε_{st} = 12.1 and ε_∞ = 10. The frequency dependence of dielectric constant can be calculated and plotted as well. All the angular frequencies are divided by 2π here, so that we can compare the predictions with experimental results. From the fig.2.6(a), we can see that for $\nu \rightarrow 0$, $\varepsilon_r = \varepsilon_{st}$. But as ν starts increasing there is a gradual increase of ε_r and it start to diverge when ν approaches ν_{T0}.

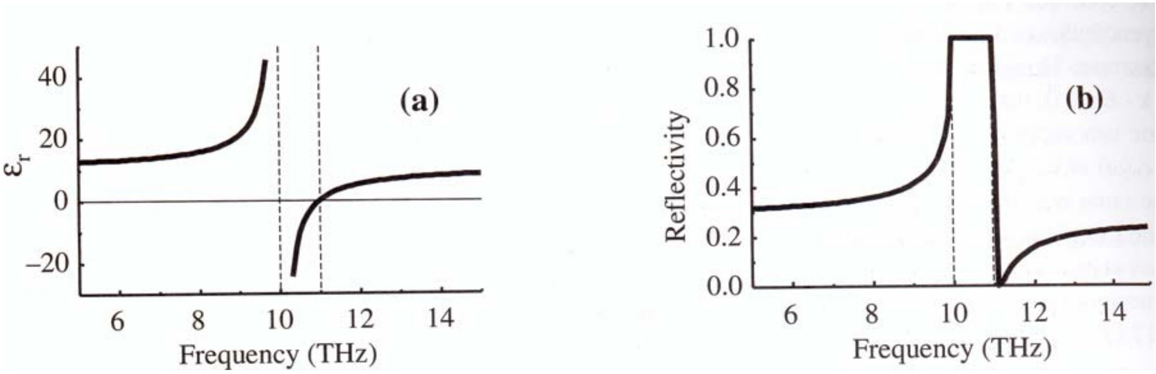

Fig.2.6. a) Frequency dependence of the dielectric constant. b) Frequency dependence of reflectivity of a crystal, where 1THz = 10^{12} Hz .

The value of ε_r is negative between ν_{T0} and ν_{L0}. Precisely at $\nu = \nu_{L0}$, ε_r is zero and then positive again, increasing asymptotically towards the value of ε_∞. We can see that in the region between ν_{T0} and ν_{L0}, the reflectivity is 100%, (see fig. 2.6), because the reflectivity is given by $R = \frac{\left|\sqrt{\varepsilon_r} - 1\right|}{\left|\sqrt{\varepsilon_r} + 1\right|}$, and $\sqrt{\varepsilon_r}$ is purely imaginary. This frequency region is called Restrahlen band.

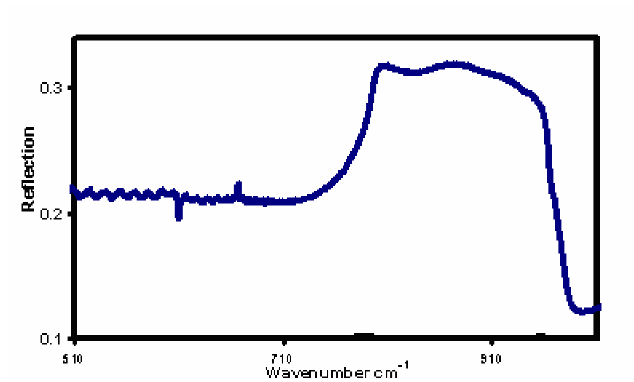

Fig.2.7. Infrared reflectivity of 4H- SiC with a pronounced Restrahlen region. A wave number of 1 cm^{-1} is equal to a frequency of 2.998 x 10^{10} Hz.

In the Restrahlen band, we expect high frequency and approximately zero transmission for real crystals. Fig.2.7 shows the experimental data for the reflectivity and transmission measurement in the 4H polytype of SiC. On comparing these experimental results (fig.2.7) with the theoretically calculated one shown in fig.2.6 (b), we see that there is general agreement between the model and the experimental data but the maximum reflectivity in the experimental curve is not 100%. This is due to the fact that we ignore the damping constant (γ) during our theoretical calculation.

3. Light Scattering Spectroscopy

When light interacts with inhomogeneous medium, it undergoes many processes. It can be absorbed, scattered, diffracted or reflected. It is well known that a perfectly homogenous medium does not scatter light; the elementary beams re-emitted from different points of such a media interfere destructively and cancel each other in all directions, except for the forward direction. However, scattering does occur in reality due to thermal fluctuations of the atoms in the media, leading to density fluctuations, so the media cannot be considered as perfectly homogenous anymore. If the inhomogeneties are of the size of the light wavelength, scattering will occur into arbitrary or well-defined direction.

For purely geometrical or local inhomogeneties with no time dependence, the scattering is elastic, which means without a change of the light energy and can occur in arbitrary directions. Depending on the size and nature of the optical inhomogeneties, the processes are called Tyndall scattering, Mie scattering, or Rayleigh scattering. For time-dependant inhomogeneties periodic in time, the scattering may also be inelastic such as those caused by phonons, sidebands to the excitation line occur. This is the case for Brillouin scattering and Raman scattering. Such scattering experiments give valuable information on the vibrational properties of the material.

3.1 Raman spectroscopy

The Raman effect arises when a photon incident on crystal is scattered inelastically due to creation or annihilation of phonon (vibrational excitation) to which a part of phonon energy is given. In contrast to the absorption spectroscopy, it is the modulation of the response of the system by vibrations, rather than the contribution of vibronic oscillators themselves.

These inelastic scattering processes can be of two types. When incident monochromatic light source of frequency ω_L interacts with crystalline material, it can excite a lattice mode or phonon state with initial population n_1 to some virtual state but as this virtual state does not correspond in general to any stationary state, it dissipates immediately, so that the phonon population remains n_1 and photon of frequency ω_L is emitted. As this emitted photon is of the same energy as the incident photon, it will correspond to elastic scattering process and is known as Rayleigh scattering as depicted in fig.3.1a. But it is also possible that the phonon will relax down to n_2 vibrational state and hence the emitted photon will have energy $\omega_{sc} = \omega_L - \omega_s$ where ω_s corresponds to energy of phonon. This process is known as Stokes process as shown in fig.3.1b. The photon scattered in this process has energy shift and we call this energy shift Raman shift and the photon scattered by this process Raman scattered photon.

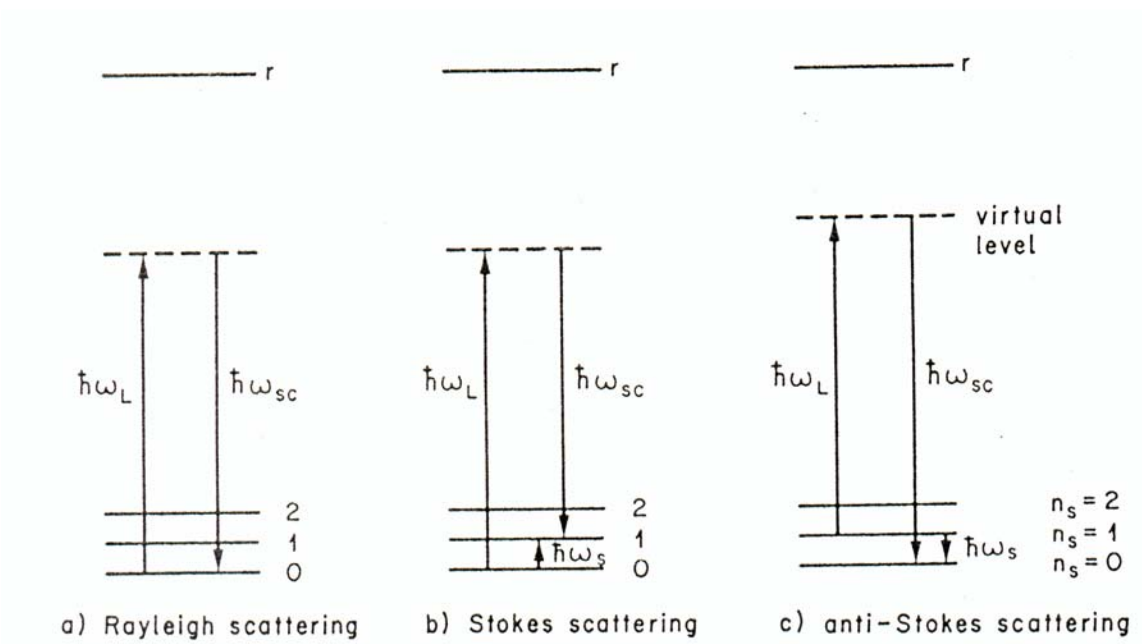

Fig.3.1. Incident photon scattered in three ways, a) Rayleigh scattering, b) first-order Stokes scattering, c) first order anti-Stokes scattering.

There is also another possibility that the phonons are already present in excited vibrational level n_2 and relax down to n_1 level when incident photons of frequency ω_L interacts. Hence the photon emitted has frequency shift of $\omega_{sc} = \omega_L + \omega_s$. This process is known as anti-Stokes process (fig.3.1c).

The anti-Stokes process is usually weaker than the Stokes process because the probability of phonons being in the higher populated state is lower than in the ground level. However at room temperature, there is still small probability of finding these phonons in excited states. In the Stokes process, the emitted photon has lower Raman shift than the one emitted in anti-Stokes process. The final energy of the photon is lower in the Stokes process than in anti-Stokes process (fig.3.2). Clearly the Raman scattering process can be viewed as either creation or annihilation of (one or more) phonons during the interaction of the light with the media.

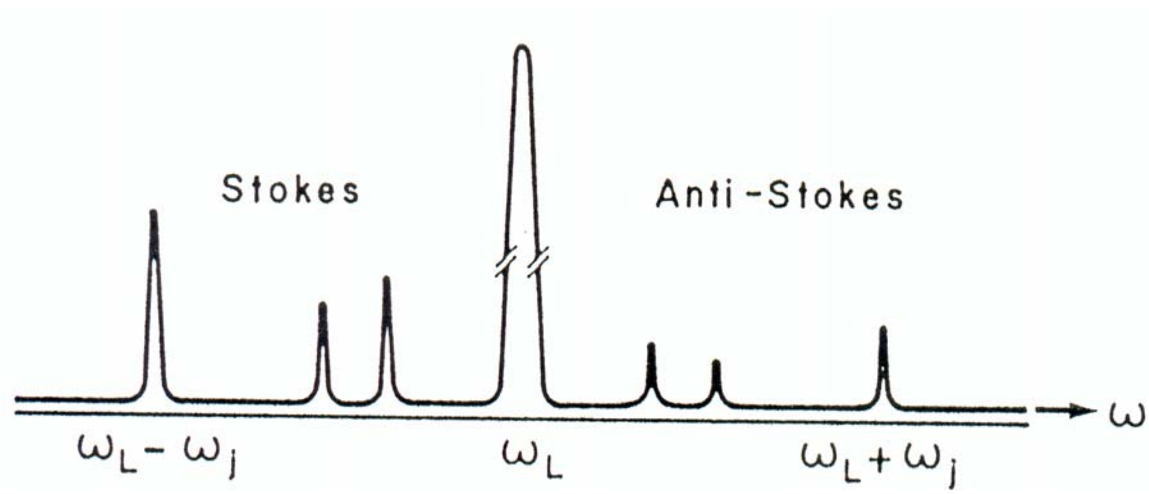

Fig.3.2. Stokes and anti-Stokes Raman spectrum (schematic). The strong line at ω_L is due to Rayleigh scattering.

Raman scattering can be of first order or higher order(if more than one phonons are involved). First order Raman scattering involves only one phonon and these phonons are only from the center of Brillouin zone due to momentum conservation and similar to the IR absorption. In Raman scattering, the incident light is scattered with relatively larger frequency shifts, independent of the scattering angle, which implies that the scattering is due to the phonons of high frequency that corresponds to optical normal modes in solids.

3.2. Instrumentation and Setup for Raman Scattering Experiment

In light scattering experiments the spectral distribution of the scattered light is analyzed relative to the spectrum of the incident light. In the case of Raman spectroscopy the changes in the spectrum are very close in energy to the energy of the incident light and many orders of magnitude smaller in intensity. Therefore a very good suppression for the elastically scattered light is required. Double or triple monochromators or Fabry- Perot interferometers can be used to filter the elastically scattered laser light. Our Raman setup consists of double monochromator, which is also quite efficient.

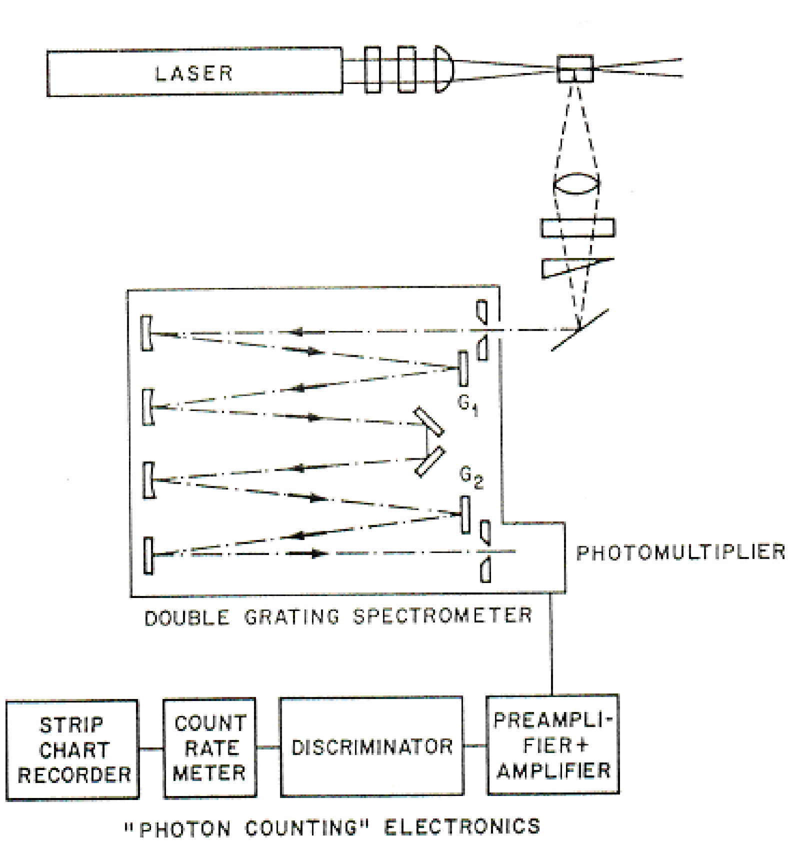

Fig. 3.3. Raman Setup

The Raman set up comprises also on Argon laser as excitation source, which is tunable to different wavelengths. The highly monochromatic laser light passes through an interference slit or a small grating monochromator that rejects the spurious lines and background from the laser source. The light beam is focused by lens and mirror on sample. We can use polarization rotator to change the polarization of laser light incident on the sample, but in our experiments, we rearrange the mirror position in order to get different polarizations of the incident laser light. Light scattered from the sample is focused by lens and passes through the polarizer. After the polarizer, the light is focused onto the entrance slit of the double monochromator. The resolution and suppression of light is highly improved compared to single monochroomator. Light leaving the exit slit of the monochromator is focused on the cathode of the photomultiplier whose output is processed with the photon counting electronics. The output is converted into digital signal and is then finally displayed on the computer. The instrumentation for Raman measurement is shown in fig.3.3.

3.3. Scattering Configuration

The intensity of Raman scattering generally depends on the mutual orientation of the direction and polarization of received light as well as of the incident light relative to the principal axes of the crystal. The variation of the scattering intensity with the experimental geometry gives information about the symmetry of the lattice vibration responsible for the observed line. Thus if the only changing component in the susceptibility tensor are xy and yx for a given lattice vibration, to observe the Raman lines due to this phonon we must arrange the polarization of the incoming laser radiation parallel to the x-axis and observed the scattered light with its polarization in the y direction and vice versa. One thus determines the Raman-active phonons with each of which we can associate a susceptibility tensor and a definite symmetry. By choosing different geometries and observing the variations in the intensity of lines due to different phonons one can in principle determine the symmetries of those phonons.

Different scattering geometries are possible for Raman experiment. The most common one is the normal back scattering (BS) configuration i.e. the laser light is made incident on the surface of the sample and the scattered light collected from the same surface as well. For uniaxial crystals back scattering geometry can be applied not only in the direction of the crystal axis but also in direction perpendicular to c-axis, which provides new information as will be seen later (see also fig.3.4).

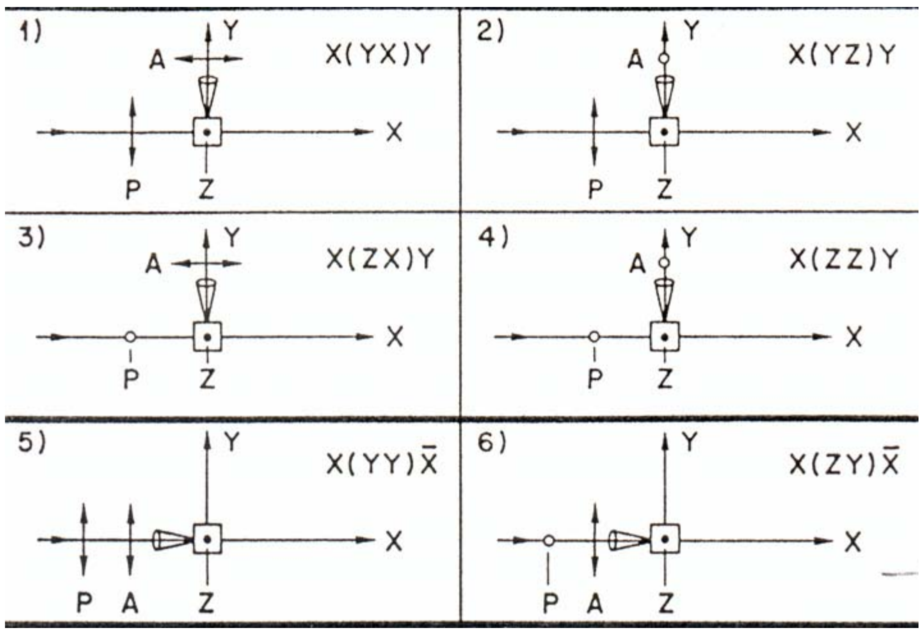

Fig.3.4. Some possible scattering geometry, we employed in Raman experiment.

There are some other scattering geometries as well like near forward scattering configuration but it is used to observe polariton and for this reason we have not used this geometry. Fig.3.4 illustrates the scattering configurations we used in our experiments. To describe a particular scattering configuration it is convenient to use the notations as described in the book by Peter Bruesch [7]. Thus for the back scattering configuration in fig.3.4, we can write $X\,(YY)\overline{X}$, where X represent the propagation direction of the wave vector k of incident light with polarization along Y direction. Similarly $\overline{X}$ represents the propagation direction of scattered light along negative X direction with polarization along Y direction.

3.4. Classical Theory of Raman scattering

In an anisotropic medium, such as an uniaxial crystal, the polarisation field **P** is not necessarily aligned with the electric field of the light **E**. In a physical picture, this can be understood, because the dipoles induced in the medium by the electric field have certain preferred directions, related to the physical structure of the crystal. Thus in general case the above two vectors are related by a tensor:

$$P = \varepsilon_0 \chi E \,, \tag{3.1}$$

where the tensor χ is the susceptibilty of crystal and it can be defined as a response of crystal as a result of interaction between electric field of photon and crystal.

Let light beam with electric field $E(t)=E_0\cos\omega_L t$ is incident on the crystal. The light field will mainly interact with the electrons in the crystal, because they are much lighter than the nuclei. Thus the main contribution to the susceptibility χ is due to the electronic polarizability. However the latter depends on the instantaneous position of the nuclei. Let us consider the situation when only one normal coordinate Q_s is excited in the lattice. If $\hbar\varpi_s$ is the phonon energy corresponding to this mode, then $Q_s = Q_{0s}\cos\omega_s t$ and the nuclei oscillate with frequency ω_s. We have also that $\chi=\chi(Q_s)$ and this function can be expressed in Taylor series as

$$\chi(Q_s) = \chi(0) + \left.\frac{\partial\chi}{\partial Q_s}\right|_{Q_s=0} Q_s + ... \approx \chi_0 + \chi_1 \cos\omega_s t \tag{3.2}$$

where in the eq.3.2, we are restricted to the first term linear in Q_s. The polarization induced by the media can thus be written as

$$P(t) = (\chi_0 + \chi_1 \cos\omega_s t) E_0 \cos\omega_L t \,. \tag{3.3}$$

In the general case, the motion of the nuclei can be represented as a linear combination of normal coordinates. Thus more generally

$$\chi(t)=\left[\left(\chi_{jl}\right)_0+\sum_k\left(\frac{\partial\chi_{jl}}{\partial Q_k}\right)_0 Q_k^0+\sum_{k,m}\left(\frac{\partial^2\chi_{jl}}{\partial Q_k\partial Q_m}\right)_0 Q_k Q_m.....\right], \qquad \textbf{(3.4)}$$

where the sum runs over all normal coordinates.

The first term in eq.3.4 represent first-order Raman effect while the second order Raman effect is given by the second term, which is quadratic in Q_k. In the following discussion, we will confine ourselves to first order Raman effect.

or

$$P(t)=\chi_0 E_0\cos\omega_L t+\left(\frac{\partial\chi_{jl}}{\partial Q_k}\right)_0 Q_k^0 E_0\left[\cos(\omega_L-\omega_s)t+\cos(\omega_L+\omega_s)t\right] \qquad \textbf{(3.5)}$$

Equation 3.5 shows that the induced polarization P oscillates not only with the frequency ω_L of the incident light, but also with the frequency $\omega_L \pm \omega_s$. These latter frequencies arise from the modulation of susceptibility by the crystal lattice oscillations.

The intensity and power spectrum of Raman scattered light is also predicted by classical radiation theory. The intensity of radiation emitted by induced polarization P(t) into the solid angle is given $d\Omega = \sin\upsilon d\upsilon d\varphi$ is given by

$$I=\frac{1}{2\pi}\int_0^\infty P(\omega)d\omega, \qquad \textbf{(3.6)}$$

where

$$P(\omega) = \pi A E_0^2 \{k_0(\omega - \omega_L) + k_1^2 \delta[\omega - (\omega_L - \omega_s)] + k_2^2 \delta[\omega - (\omega_L + \omega_s)]\}. \quad \textbf{(3.7)}$$

The power spectrum illustrated by eq 3.6 is shown in fig.3.5. Thus classical theory correctly predicts the occurrence of Stokes and anti-Stokes process but leads to an incorrect ratio of intensities.

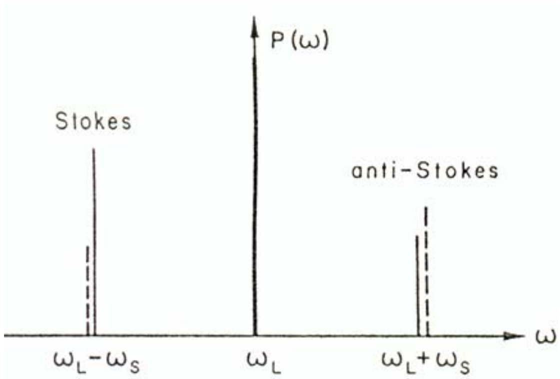

Fig.3.5. Intensity of Stokes and anti-Stokes line by classical theory.

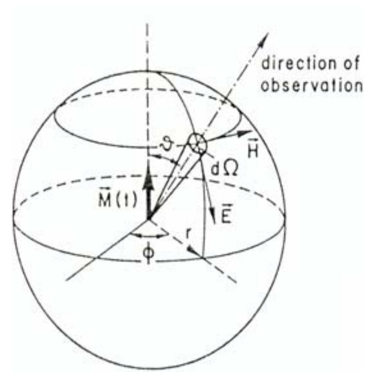

Fig.3.6 Polarization of the radiation emitted by an oscillating electric dipole P(t). E and H are the field vectors of the radiation propagating in direction of observation

The ratio of intensity of Stokes and anti-Stoked process calculated by classical model is

$$\frac{I_{Stokes}}{I_{anti-Stokes}} = \frac{(\omega_L - \omega_s)^4}{(\omega_L + \omega_s)^4} \quad . \quad \textbf{(3.8)}$$

which will be less than one and where as experiment shows that Stokes lines are more intense than the anti-stokes ones. This inconsistency is eliminated by Quantum theory of Raman scattering, which lead to intensity ratio

$$\frac{(\omega_L - \omega_s)^4}{(\omega_L + \omega_s)^4} \propto \exp\left(\frac{\hbar\omega}{k_B T}\right). \quad \textbf{(3.9)}$$

where k_B is the Boltzmann constant and T is the temperature. The ratio given in eq.3.9 is considerably larger than unity in contrast to eq (3.8) for the classical case.

3.4.1. Classical determination of the Raman Tensor

The relation $P(t) = \chi_0 E(t)$ is vectorial relation and in general the direction of P does not coincide with the direction of the electric field E. If we consider only first order Raman scattering,

$$\chi_{jl} = (\chi_{jl})_0 + \sum_k \left(\frac{\partial \chi_{jl}}{\partial Q_k} \right)_0 Q_k$$

Here $\partial\chi_{jl}/\partial Q_k$ is a component of derived susceptibility tensor. This tensor is also known as Raman tensor and often written as $\chi_{jlk,}$ $(\chi_{jl})_k$ or $\chi_{jl,k}$. The component of the Raman tensor has three indices. j and ℓ extends over the coordinates 1 to 3 and k runs over the the 3N-3 normal coordinates of the vibrations, where N is the number of atoms per unit cell. In other words k run over all modes with wave vector k = 0. The Raman tensor which refers to all zone center vibrations thus has rank three. For an individual mode this tensor is given by a matrix with three rows and three columns whose components are the derivatives of the susceptibilty. So in matrix form we can write:

$$\begin{pmatrix} P_x \\ P_y \\ P_z \end{pmatrix} = \begin{pmatrix} \chi_{xx} & \chi_{xy} & \chi_{xz} \\ \chi_{yx} & \chi_{yy} & \chi_{yz} \\ \chi_{zx} & \chi_{zy} & \chi_{zz} \end{pmatrix} \begin{pmatrix} E_x \\ E_y \\ E_z \end{pmatrix} , \qquad \textbf{(3.10)}$$

or

$$P_j = \sum_l \chi_{jl} E_l \quad , \qquad \textbf{(3.10a)}$$

where χ is a symmetrical tensor, that is

$$\chi^T = \chi$$
$$or \qquad \textbf{(3.11)}$$
$$\chi_{jl} = \chi_{lj}$$

It can be further shown as well that there exists a coordinate system with axes (x′,y′,z′) such that the relation between P and E, when reffered to these axes, assumes a simple form.

$$\begin{pmatrix} P'_{x'} \\ P'_{y'} \\ P'_{z'} \end{pmatrix} = \begin{pmatrix} \chi_{x'x'} & 0 & 0 \\ 0 & \chi'_{y'y'} & 0 \\ 0 & 0 & \chi_{z'z'} \end{pmatrix} \begin{pmatrix} E_{x'}{}' \\ E'_{y'} \\ E'_{z'} \end{pmatrix} \qquad \textbf{(3.12)}$$

or

$$P' = \chi' E' \qquad \textbf{(3.12a)}$$

where χ′ is a diagonal matrix. Such axes are called principle axis of the susceptibility. One of the principle axis of the susceptibilty always coincides with the symmetry axis of symmetrical system and is always perpendicular to a plane of symmetry.

The transformation from one coordinate system (x,y,z) to another (x′,y′,z′) takes place through an orthogonal matrix R, where $R^{-1}=R^T$, and we can write

$$P' = RP = R\chi E = \chi' E' = \chi' RE \,,$$

or

$$\chi = R^T \chi' R \,.$$

If we consider a system in equilibrium configuration, then the components of χ are

$$\chi_{jl} = \delta_{jl}\chi_{jl}^{(0)} .$$

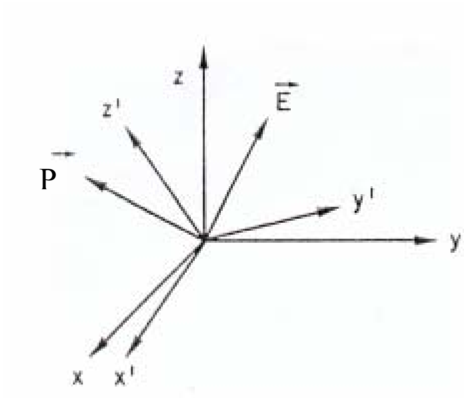

Fig.3.7. Coordinate system (x,y,z), identical with the laboratory system and principal axes system of susceptibility, (x´, y´,z´). P is the dipole moment induced by the electric field E of the light.

If as a result of thermal fluctuations the system is in a distorted configuration there will be a new coordinate system (x′,y′,z′) shown in fig.3.7 which in general will not coincide with (x,y,z). For such a system we can expand χ_{jl} in terms of normal coordinates Q_k as in eq 3.3 and obtain

$$\chi_{jl} = \chi_{jl}^{(0)} + \sum_k \chi_{jl,k} Q_k + \frac{1}{2}\sum_{k'k''} \chi_{jl,k'k''} Q_{k'} Q_{k''} + \ldots\ldots\ldots, \qquad \textbf{(3.13)}$$

where $\chi_{jl}^{(0)}$ represent the susceptibility of the system in equilibrium.

For a given normal coordinate Q_k we may define the changes in susceptibility components

$$\Delta\chi_{jl,k} = \chi_{jl,k} Q_k = \left(\frac{\partial \chi_{jl}}{\partial Q_k}\right)_0 Q_k \qquad \textbf{(3.14)}$$

and a matrix with elements

$$\chi_{jl,k} = \left(\frac{\partial \chi_{jl}}{\partial Q_k} \right)_0 \quad , \qquad \text{namely} \tag{3.15}$$

$$\delta\chi^{(k)} = \begin{pmatrix} \chi_{xx,k} & \chi_{xy,k} & \chi_{xz,k} \\ \chi_{yx,k} & \chi_{yy,k} & \chi_{yz,k} \\ \chi_{zx,k} & \chi_{zy,k} & \chi_{zz,k} \end{pmatrix} \tag{3.16}$$

If we replace χ (susceptibility) by α (polarisability) these expressions can be considered as a generalization for a molecule. From the previous considerations, we can deduce that the lattice mode will be Raman active if one of the six components of $\chi_{jl,k}$ of matrix $\delta\chi^{k}$ is different from zero. If this is the case, the mode Q_k is Raman active. The appearance of Raman mode in any experiment is dependant upon the symmetry of the equilibrium configuration and of the modes Q_k. Active and inactive Raman modes in Silicon carbide are dicussed in next chapter.

3.5. Quantum Theory of Raman Scattering

The complete quantum theory of Raman scattering is complex and rather lengthy. This section presents just a basic review with respect to the first order Raman scattering. According to the corpuscular theory of light, Rayleigh scattering corresponds to an elastic collision process between photon and the crystal whereas the Raman scattering corresponds to the inelastic collision of photons with crystal with the emission (Stokes process) or absorption (anti-Stokes) of phonons.

3.5.1. First- Order Raman Scattering

In first-order Raman scattering, only one phonon is involved; this correspond to term linear in Q_k in eq.3.3. Fig 3.1 shows the transition for Rayleigh scattering and for first - order Stokes and anti-Stokes scattering. Let ω_L, k_L be the frequency and wavevector of incident photon and ω_s, k_s be frequency and wavevector of scattered photon and ω, k of the optical phonon. Energy and momentum are conserved between initial and final state of system.

For Rayleigh scattering,

$$\omega_L = \omega_s,$$
$$k_L = k_s. \tag{3.17}$$

For Raman scattering the conservation of energy and momentum yields:

$$\omega_L = \omega_s \pm \omega\ , \tag{3.18}$$

$$k_L = ks \pm q\ . \tag{3.19}$$

where the (+) sign indicates that phonon ω(q) is created in Stokes process while in the anti-Stokes process the phonon ω(q) is annihilated.

The two processes are shown schematically in fig.3.1. Since $\omega_L >> \omega_s = \omega(k)$ it follows from eq.3.18 that $\omega_L \cong \omega_s$. since k_L and ks are the wavevectors within the crystal, we have $k_L = 2\pi/\lambda_L$, $k_s = 2\pi/\lambda_s$ where $\lambda_L = \lambda_{vac} /n\ (\omega_L)$, $\lambda_s = \lambda_{vac} /n\ (\omega_s)$ (λ_{vac}: wavelength in vacuum). Since $\omega_L \cong \omega_{s,}$ it follows that $k_L \cong k_s$. In addition, since λ_L and λ_s are much larger than the lattice parameter a, hence k_L and k_s are much smaller than π/a, the magnitude of wavevector at the zone boundary. Therefore from eq.3.11 it follows that

$q \ll \pi/a$, that implies that optical modes with $q \cong 0$ can only be involved in first order Raman scattering.

4. Group Theoretical Consideration of the 4H and 6H Polytypes of SiC

In this chapter, we will provide in more detail the group theoretical analysis necessary to understand the experimental results. We will be concerned with the symmetry analysis of the phonons near the Γ and M point of the Brillouin zone, zone folding in higher polytypes, theoretical prediction of modes in different scattering configurations and assignment of representation to Raman and IR absorption lines in spectra obtained experimentally by theoretical arguments.

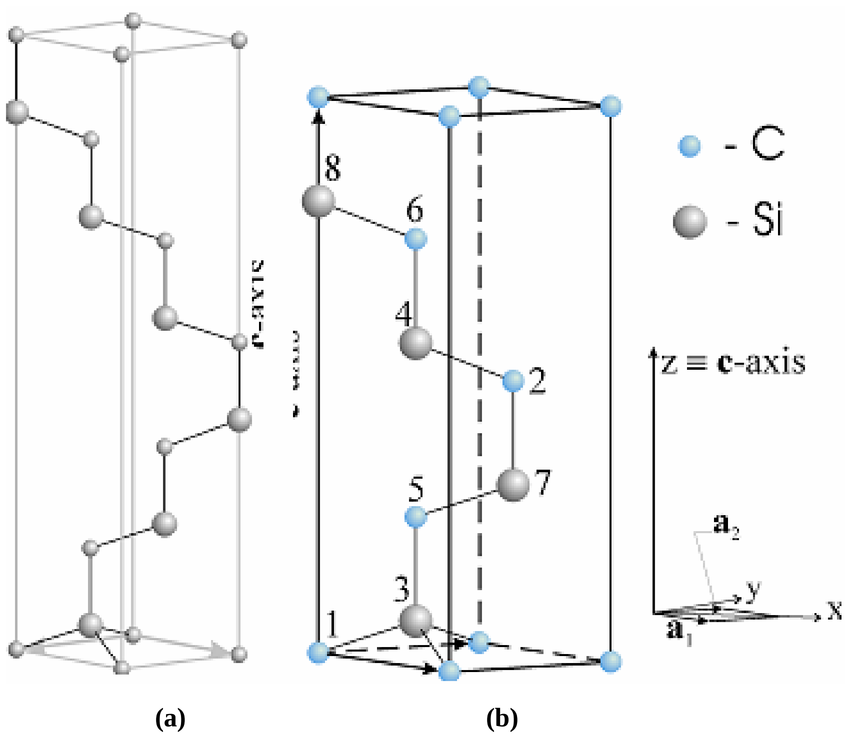

Fig.4.1. a) unit cell of 6H-SiC, b) unit cell of 4H-SiC. The atoms in 4H-SiC unit cell are enumerated in such a way that the pair of subsequent numbers (1,2), (3,4), (5,6), (7,8) denote equivalent atoms.

4.1. Classification of Symmetry of Phonons for different directions of the wave vector K_{pnonon} in the Brillouin Zone of 4H & 6H-SiC.

4H-SiC has 8 atoms per unit cell while 6H-SiC has 12 atom in one cell (see fig 4.1). In fig 4.1, the atoms are labeled in such a way that subsequent numbers (e.g. 1 and 2) correspond to equivalent atoms. 4H and 6H-SiC, both hexagonal polytypes of SiC belong to C_{6v}^{4} space symmetry group, which contains altogether 12 operations which will satisfy the symmetry condition for these crystals as described in table.4.1. We will consider table.4.1 in detail in later paragraphs.

In general, the number of phonon branches in any crystal is 3N where N is number of atoms per unit cell. Out of these 3N modes, three are acoustic modes and 3N-3 optical modes. Some of these optical and acoustic modes are degenerate in certain directions of the Brillouin zone. They are usually classified into transverse and longitudinal modes. Only the optical modes have non-vanishing energies at the centre of the Brillouin zone ($k \approx 0$). The hexagonal and rhombohedral poltypes of SiC have well defined c-axis. So the longitudinal modes (along c-axis) are also termed as axial modes and transversal modes (⊥ to c-axis) as planar modes. This classification of modes into axial and planar modes is quite specific and is valid only for particular scattering geometry. Later we will see that this classification of modes requires modification for different scattering geometries. But now for the moment, we will consider this classification of modes as described above.

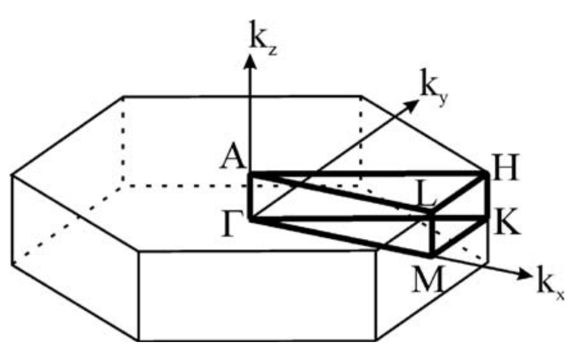

Fig.4.2. First Brillouin zone of 4H and 6H-SiC

These axial and planar modes are long wavelength modes corresponding to wave vector k≈0 or phonon modes at the centre of the Brillouin zone (Γ-point). The Brillouin zone (BZ) of 4H and 6H-SiC is shown in fig.4.2. In fig.4.2, the Γ- point represents the centre of BZ where Γ to A - point represents the direction along c-axis (parallel to z-axis) in the BZ. Γ to K and Γ to M point represent directions in the x-y plane of crystal (i.e. the basal plane). So the axial modes are along Γ- A and planar modes are along Γ-M or Γ-K direction in BZ (general case).

The total number of lattice modes, according to the above discussion, is 24 for 4H and 36 for 6H. Out of these 24 modes in 4H, 21 will be optical modes and 3 will be acoustic modes. However, not all optical modes are active in IR absorption or Raman scattering. Our purpose will be to classify the phonons near the zone center Γ by symmetry, and then find the symmetries of the phonons active in IR and Raman. Subsequently, we will use the specific tensors representing the susceptibility derivatives for the phonons of each allowed symmetry in order to label the lines experimentally observed in our Raman and IR spectra.

It is well known using group theory that the phonons at a certain point in BZ can be classified by symmetry, that is, every phonon can be labeled with one of the irreducible representations of the group of the wavevector k. The group of wave vector K_A in the direction Γ- A of the Brillouin zone is C_{6v} but in the direction Γ- M, the group of wavevector is C_{2v}. By definition, this is the subgroup of the point group of the crystal (C_{6v} in our case), which contains those operations, which leave the wave vector invariant possibly changing only its direction from $\vec{K}\, to - \vec{K}$. Thus it is easy to see, that if the wave vector is in direction towards the M point (K_M), the group of the wave vector is C_{2v}.

K_{phonon} denotes the wave vector of phonon created or annihilated in Raman Stokes and anti-Stokes process. Using the conservation of energy and momentum laws, we can draw the directions of the phonon wave vector for different scattering geometries. The different directions of the phonon wave vector have to be analyzed using different point groups, which will then correspond to modes with different symmetries in certain measured geometries for these polytypes. For example, for certain geometry, if the direction of resultant or phonon wave vector is along c-axis (Γ- A), the C_{6v} point group can predict the crystal modes but if the resultant wave vector is perpendicular to the crystal axes (in Γ-M or Γ-L direction), the point group is C_{2v}.We will discuss the direction of phonon wave vector for different measuring geometries in detail in later paragraphs.

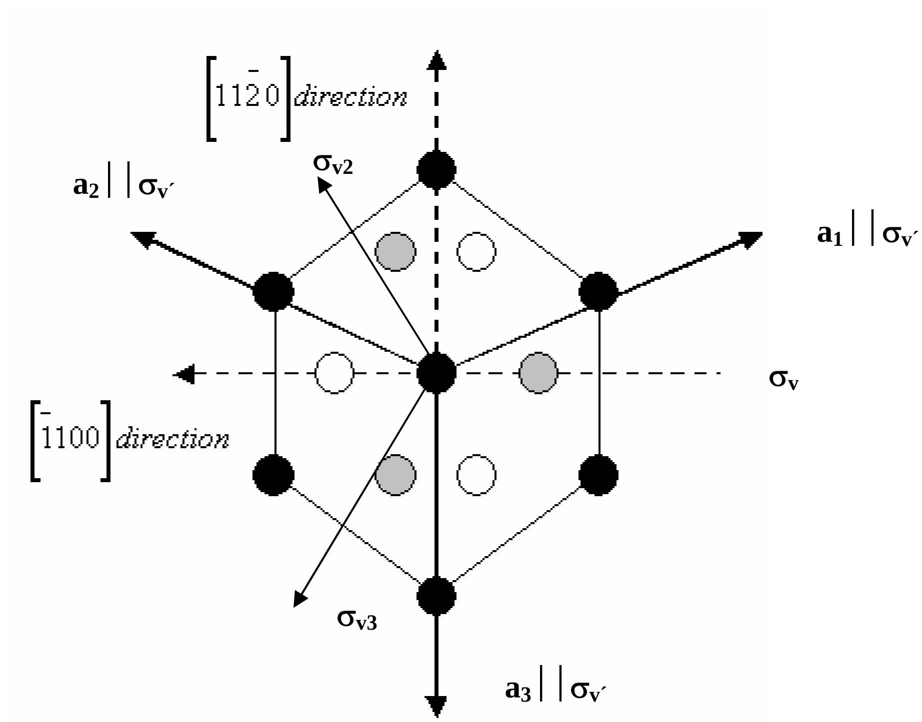

Fig.4.3. Reflection operation σ_v and $\sigma_{v'}$

Let us consider table.4.1 in detail first. In table.4.1, the first row represents the rotational operation (3x3) matrices included in the C_{6v} point group. The first operation 'E` is identity operation, $2C_6$ represent the rotations operation by 180^0 and $(180^0)^{-1}$, $2C_3$ are rotations by 120^0, C_6 by 60^0. All rotations are about the Γk_z axis, corresponding to c-axis direction in the direct space. $3\sigma_v$ and $3\sigma_{v'}$ are six reflection operations across planes rotated by 120^0 from each other about the c-axis of the crystal as shown in fig.4.3. The operation σ_v is equivalent to the AΓML plane and $\sigma_{v'}$ is $\perp$ to Γk_x.

The E, $2C_3$ and $3\sigma_v$ operations alone will bring the crystal into itself, and are totally symmetric operations however the operations, $2C_6$, C_2 and $3\sigma_{v'}$ require an additional translation by half the height of the unit cell along the c-axis, i.e.τ = ½ c in order to bring to bring the crystal into itself. The total number of operations is equivalent to the order of group. Hence the order of group for C_{6v} is 12. The group has six irreducible representations among which four are one dimensional, and two-2 dimensional. The column on the left side of the table.4.1 represents the notations for these irreducible representations. The remaining columns represent the characters of the representations for different operations. For example A_1 modes has character 1 for all operations, while E_1 modes have character 2 for identity operation, etc.

Table.4. 1. Character table of C_{6v} point group.

C_{6v}	E	$2C_6$	$2C_3$	C_2	$3\sigma_v$	$3\sigma_v'$
A_1	+1	+1	+1	+1	+1	+1
A_2	+1	+1	+1	+1	- 1	- 1
B_1	+1	- 1	+1	- 1	+1	- 1
B_2	+1	- 1	+1	- 1	- 1	+1
E_1	+2	+1	- 1	- 2	0	0
E_2	+2	- 1	- 1	+2	0	0

The point group C_{2v} is a subgroup of C_{6v} and contains four of the 12 symmetry operations of C_{6v}, namely, E (the identity transformation), C_2, σ_v and $\sigma_{v'}$. C_2 is equivalent to the Γk_z axis, σ_v equivalent to AΓML plane, and $\sigma_{v'}$ is $\perp$ Γk_x. The four irreducible representations of C_{2v} are all one-dimensional and are listed in table.4.2. Thus, there is no symmetry-based degeneracy of the phonon energies in the Γ-M and Γ-K direction, and the matrix representations are identical to the characters.

Table.4. 2. Character table of C_{2v} point group.

C_{2v}	E	C_2	σ_v	σ_v'
A_1	+1	+1	+1	+1
A_2	+1	+1	- 1	- 1
B_1	+1	- 1	+1	- 1
B_2	+1	- 1	- 1	+1

The group-theoretical technique for determination of the number of phonons of given symmetry at Γ point (A_1, A_2, B_1, B_2, E_1, E_2) and M point (A_1, A_2, B_1, B_2) is described in detail in ref [13,14]. So here we will give a brief summary of the application of that technique to our particular case.

For the 4H polytype, a 24-dimensional representation Γ^{disp} (called the displacement representation) can be constructed in the following way. Let us consider a 24-dimensional vector 'c' for 4H-SiC, (for 6H-SiC, it will be 36 dimensional), the first three components of which are the x, y and z projections of the displacement of atom No 1, the next three components are the corresponding projections of the atom No 2, etc. Let us think of each symmetry operation as acting on the displacements of atoms, instead of on the atoms themselves. Then the result of the symmetry operation T on the vector c will be another vector c′, which can be written as $c' = \Gamma^{disp}(T).c$. Obviously, the set of matrices $\{\Gamma^{disp}(T),\ T \in C_{6v} \text{ or } C_{2v}\}$ forms a (reducible) representation of the group of the wave vector (C_{6v} or C_{2v} in our case), and it is quite straightforward to see that this representation can be presented as a direct matrix product

$$\Gamma^{disp}\left(T\right) = p(T) \otimes R(T) \qquad \textbf{(4.1)}$$

where p(T) is the so called permutation matrix for the operation T (the permutation matrix is a matrix containing 0's and 1's, and storing information about where each atom is going when the crystal is subjected to the operation T). The permutation matrix has NxN dimension generally, where N is the number of atoms per unit cell. R(T) is the ordinary 3x3 orthogonal matrix representing the rotation corresponding to the operation T. Both sets {p(T)}(eight dimensional for 4H-SiC and 12 dimensional for 6H-SiC), and {R(T)} (three dimensional) form also representations called permutation and vector representations, respectively.

The matrices for the rotational operations of C_{6v} (and C_{2v}) groups are as follow:

$$R(C_6) = \begin{pmatrix} 1/2 & -\sqrt{3}/2 & 0 \\ \sqrt{3}/2 & 1/2 & 0 \\ 0 & 0 & 0 \end{pmatrix}, R(C_3) = \begin{pmatrix} -1/2 & -\sqrt{3}/2 & 0 \\ \sqrt{3}/2 & -1/2 & 0 \\ 0 & 0 & 0 \end{pmatrix},$$

$$R(C_2) = \begin{pmatrix} -1 & 0 & 0 \\ 0 & -1 & 0 \\ 0 & 0 & 1 \end{pmatrix},$$

where

$$R(C_3)^{-1} = R(C_3)^T$$
$$R(C_6)^{-1} = R(C_6)^T$$

$$R(\sigma_v) = \begin{pmatrix} 1 & 0 & 0 \\ 0 & -1 & 0 \\ 0 & 0 & 1 \end{pmatrix}, R(\sigma_{v2}) = \begin{pmatrix} -1/2 & -\sqrt{3}/2 & 0 \\ -\sqrt{3}/2 & 1/2 & 0 \\ 0 & 0 & 1 \end{pmatrix}, R(\sigma_{v3}) = \begin{pmatrix} -1/2 & \sqrt{3}/2 & 0 \\ \sqrt{3}/2 & 1/2 & 0 \\ 0 & 0 & 1 \end{pmatrix}$$

$$R(\sigma_{v'}) = \begin{pmatrix} 1/2 & \sqrt{3}/2 & 0 \\ \sqrt{3}/2 & -1/2 & 0 \\ 0 & 0 & 1 \end{pmatrix}, R(\sigma_{v_2}{}') = \begin{pmatrix} 1/2 & -\sqrt{3}/2 & 0 \\ -\sqrt{3}/2 & -1/2 & 0 \\ 0 & 0 & 1 \end{pmatrix}, R(\sigma_{v_3}{}') = \begin{pmatrix} -1 & 0 & 0 \\ 0 & 1 & 0 \\ 0 & 0 & 1 \end{pmatrix}.$$

For rotational operations E, C_3 and σ_v, which do not involve translations, the unit cell together with each atom position remain unaltered and the permutation matrix for 4H-SiC has the form

$$p(E, C_3, \sigma_v) = \begin{pmatrix} 1 & 0 & 0 & 0 & 0 & 0 & 0 & 0 \\ 0 & 1 & 0 & 0 & 0 & 0 & 0 & 0 \\ 0 & 0 & 1 & 0 & 0 & 0 & 0 & 0 \\ 0 & 0 & 0 & 1 & 0 & 0 & 0 & 0 \\ 0 & 0 & 0 & 0 & 1 & 0 & 0 & 0 \\ 0 & 0 & 0 & 0 & 0 & 1 & 0 & 0 \\ 0 & 0 & 0 & 0 & 0 & 0 & 1 & 0 \\ 0 & 0 & 0 & 0 & 0 & 0 & 0 & 1 \end{pmatrix},$$

where 1's at the diagonal represent position of atoms in 4H-SiC after applying rotational operation. Thus atom 1 remains in the position of atom 1,etc.

The permutation matrix for the rotational operations C_2, C_3 and $\sigma_{v'}$, which require translation by half of the length of 'c' afterwards to bring the crystal into itself position has the form:

$$p(C_2, C_6, \sigma_v') = \begin{pmatrix} 0 & 1 & 0 & 0 & 0 & 0 & 0 & 0 \\ 1 & 0 & 0 & 0 & 0 & 0 & 0 & 0 \\ 0 & 0 & 0 & 1 & 0 & 0 & 0 & 0 \\ 0 & 0 & 1 & 0 & 0 & 0 & 0 & 0 \\ 0 & 0 & 0 & 0 & 0 & 1 & 0 & 0 \\ 0 & 0 & 0 & 0 & 1 & 0 & 0 & 0 \\ 0 & 0 & 0 & 0 & 0 & 0 & 0 & 1 \\ 0 & 0 & 0 & 0 & 0 & 0 & 1 & 0 \end{pmatrix},$$

According to it, atom 1 goes to the position of atom labeled 2 and vice versa. It is also true for other subsequent pair of atoms (see fig.4.1). The rotational matrices described before can be written in place of the non-zero entries in the permutation matrix to form a 24 dimensional displacement representation Γ^{disp} for 4H-SiC. We can also write the permutation matrices for 6H-SiC, which will have the same forms. The only difference will be the dimension of matrix (i.e.12x12 matrix) because of 12 numbers of atoms in the unit cell of 6H-SiC.

Hence after applying the operation T, we can say that the c-axis will transform into itself, i.e.

$$c' = \Gamma^{disp}(T).c \tag{4.2}$$

where Γ^{disp} have the form given in eq.4.1 for operations E, C_3 and σ_v and this is true for all operations T of the point group C_{6v}.

We can now calculate the number of phonons (n_p) transforming as each of the irreducible representations of either C_{6v} (for Γ-A) or C_{2v} (for Γ-M, Γ-K phonons) by using the well-known magic counting formula [9].

$$n_p = \frac{1}{g} \sum_{\mathrm{T} \in C_{6v}, C_{2v}} \chi^{disp}(T) \chi^{p}(T)^{*} \tag{4.3}$$

where n_p is the number of phonon modes of symmetry Γ_p (any of the irreducible representation), g is the order of the group, which is 12 for C_{6v} and 4 for C_{2v}. $\chi^{disp}(T)$ is the character of $\Gamma^{disp}(T)$ and $\chi^{p}(T)^{*}$ is the complex conjugate of the characters of the irreducible representations of C_{6v} and or C_{2v}. In our case all characters of irreducible representations for both groups are real and hence the complex conjugate has no effect.

The total number of phonons at Γ point for C_{6v} group is

$$\Gamma^{disp} = 4A_1 + 4B_1 + 4E_1 + 4E_2 \tag{4.4}$$

Hence there are 16 distinct modes but since E_1 and E_2 modes are double degenerate, the total number is 24, as expected. Among these, three are acoustic, describing translation of the unit cell (or of the crystal) as a whole, that is, the displacements of all atoms are in the same direction and equal. Since a single vector represents all displacement for the acoustic modes, it must transform in accord with the rotational representation defined by the matrices R(T). Using eq.4.3, we obtain by analogy with eq.4.4 that R(T) decomposes into irreducible representations in the following way:

$$R = A_1 + E_1 \tag{4.5}$$

Consequently, one of the four A_1 modes and one of the E_1 modes are acoustic (three in total as E_1 modes are doubly degenerate). Thus, for the optic modes one obtains:

$$\Gamma^{optical} = 3A_1 + +4B_1 + 3E_1 + 4E_2 \tag{4.6}$$

Modes allowed in IR spectroscopy are:

$$IR - Active : 3A_1 + 3E_1 \tag{4.7}$$

Similarly, it can be shown that the Raman active modes are those whose symmetries can be found in the decomposition of the direct product $R \otimes R$ that leads to the result

$$Raman - Active : 3A_1 + 3E_1 + 4E_2 \tag{4.8}$$

The total number of phonons at M point for C_{2v} point group calculated using magic counting formula given in eq.4.3 is

$$\Gamma^{disp} = 8A_1 + 4A_2 + 4B_1 + 8B_2$$

(4.9)

Out of these 24 modes for C_{2v} group 21 will be optical and 3 will be acoustic modes, which can be found to have A_1+ B_1+B_2 symmetries, therefore,

The IR active optical modes are

$$IR - Active : 7A_1 + 3B_1 + 7B_2$$

(4.10)

and the Raman active optical modes are

$$Raman - Active : 7A_1 + 4A_2 + 3B_1 + 7B_2$$

(4.11)

Eq.4.11 depicts that all modes are Raman active, if the experimental geometry is such that the phonon wavevector is along the Γ-M direction. So the general relation can be formulated to calculate the number of modes in NH polytype (N=4,6 for 4H and 6H-SiC respectively).

The total number of IR active optical modes for C_{6v} is

$$(N-1)(A_1 + E_1) \quad \textbf{(4.12)}$$

For Raman Spectroscopy, the total number of Raman-active optical modes for C_{6v} group is

$$n_p = 5N - 3 = (N-1)A_1 + (N-1)E_1 + NE_2 \quad \textbf{(4.13)}$$

Similarly we can formulate a general formula for C_{2v} point group. IR optical modes in C_{2v} are

$$(2N-1)(A_1+B_2)+(N-1)B_1 \quad \textbf{(4.14)}$$

Allowed optical Raman modes can be calculated by the general formula

$$(2N-1)(A_1+B_2)+4A_2+(N-1)B_1 \quad \textbf{(4.15)}$$

4.1.1. Zone Folding

Different polytypes of SiC have different lattice periods along the c-axis and the polytype with the shortest period is 3C-SiC (β-SiC), which has the zinc-blende structure. The notation α-SiC is often used to denote the NH or 3NR polytypes that contain N formula units (Si-C). The unit cell length of these α-type polytypes along the c-axis is N times larger (corresponding to the <111> direction of zinc-blende structure) than that of the basic polytype (3C-polytype). Hence the BZ in Γ-L is reduced to the 1/N of the basic Brillouin zone, i.e., minizone. The phonon dispersion curves of 3C, 4H and 6H-SiC in the <111> direction, corresponding to Γ-A direction in the BZ is shown in fig4.4, illustrating the zone-folding concept.

The dispersion curves of the phonon modes propagating along the c-direction in higher polytypes are approximated by folded dispersion curves in the basic Brillouin zone as shown in fig.4.4 This zone folding along the [00ξ] direction provides a number of new phonon modes at the Γ point (k=0), which correspond to the phonon modes inside or at the edge of the basic Brillouin zone. The phonon modes arising from the zone folding are called ´folded modes’. The unit cell of 3C-SiC contains one formula unit and there is one LO mode and a doubly degenerate TO mode in the optical branches (see fig.4.4). A folded mode corresponds to a phonon mode with a reduced wave vector $x = k/k_B = 2m/N$ along the <111> direction in the basic Brillouin zone of the 3C-SiC, where m is an integer less than or equal to N/2 ($m \leq N/2$) and k_B is a wave vector of the zone edge in the basic Brillouin zone.

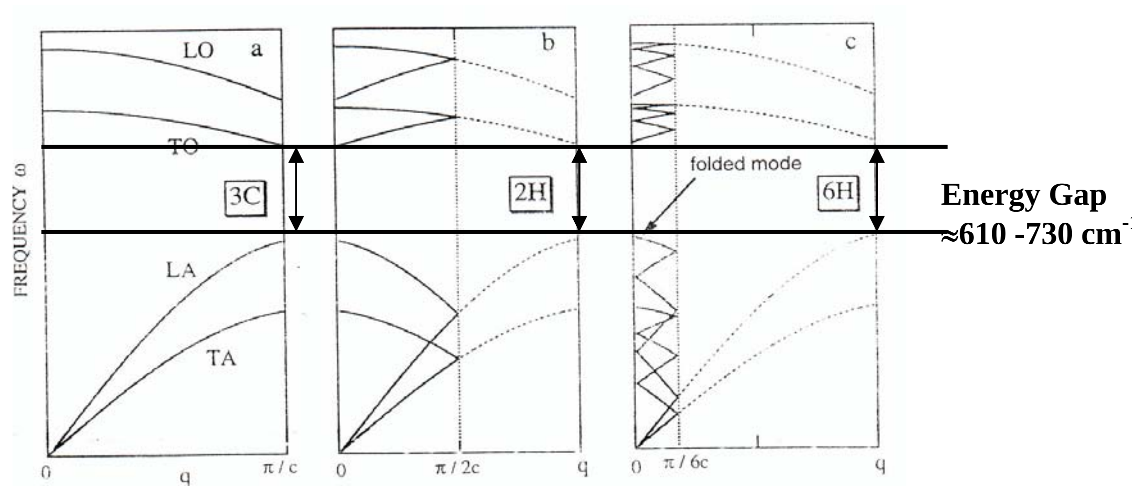

Fig.4.4.The phonon dispersion of: a 3C-SiC in the Basic (large) BZ; b & c) 2H and 6H-SiC in the corresponding minizones, showing the folded modes [15].

4.1.2. Geometrical Considerations

The direction of the resulting K_{phonon} wave vector is very important to be considered for different geometry. When the wave vector of the phonon is exactly parallel to the c-axis of the crystal, i.e. K_{phonon} || Γ-A direction in BZ, the group of the wave vector is C_{6v} and it is C_{2v} when the wave vector K_{phonon} is perpendicular to the c-axis, i.e. K_{phonon}||Γ-M or Γ-K directions in the BZ. When the K_{phonon} is neither parallel nor perpendicular to c-axis but has some intermediate angle with respect to c-axis, i.e. K_{phonon}||Γ-A-M plane in BZ, the wave vector group is C_s for 4H and 6H-SiC. It can be seen from fig 4.5 that wave vector K_{phonon} is parallel to c-axis i.e. $\theta = 0^0$ (along z-axis) only in the case of back scattering geometry from surface and is perpendicular i.e $\theta = 90^0$ (along x-axis) for back scattering geometry from edge. K_{phonon} has intermediate angle with c-axis in both cases of rectangular geometry i.e. $\theta = 45^0$ (zx-plane). Hence different point groups for different geometries will predict the modes.

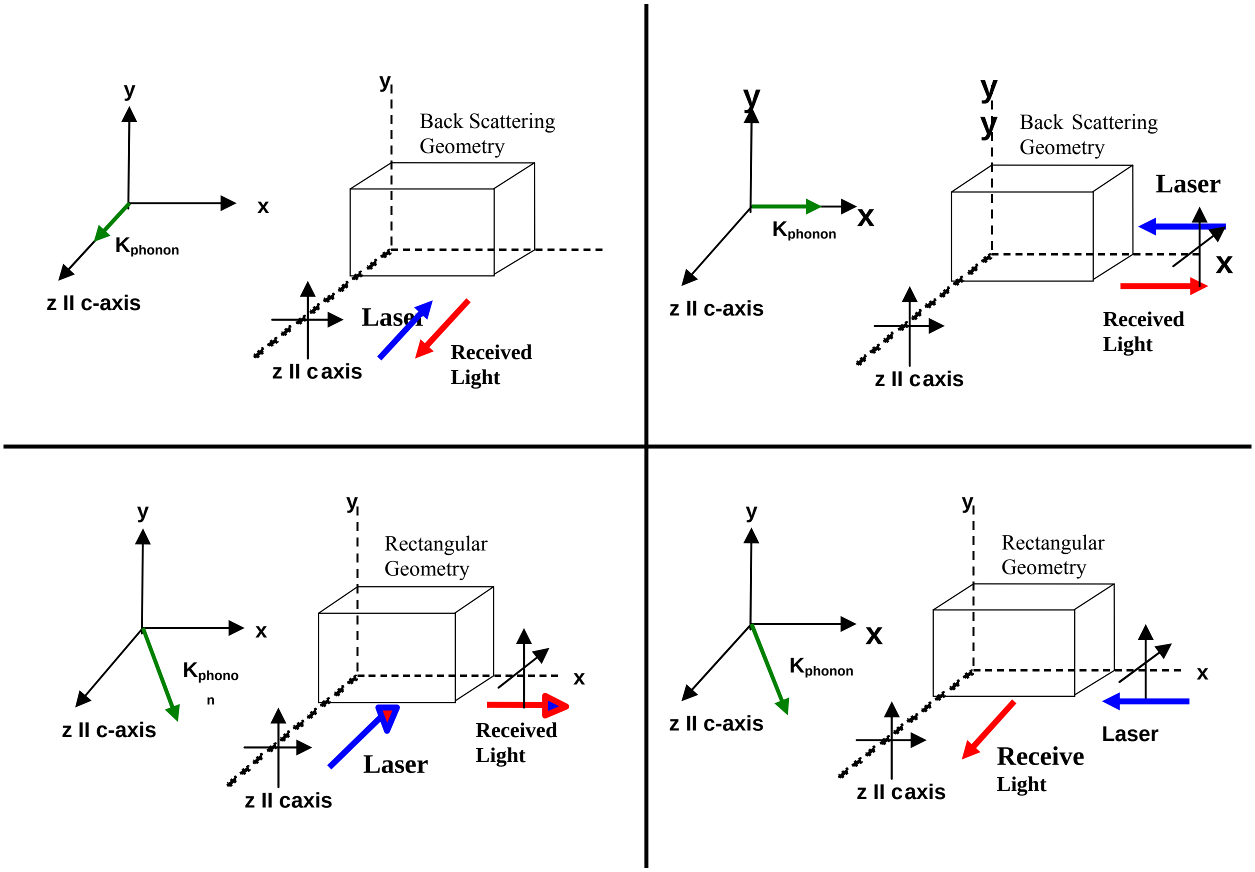

Fig.4.5. Four different experimentally measured geometries a) Rectangular geometry(E_L through surface, E_r through edge), b) Rectangular geometry(E_L through edge, E_r through surface), Back Scattering (edge), Back Scattering (surface).

We have already discussed the point group C_{6V} and C_{2V}. The point group C_s is quite simple group and the characters are given in table.4.3. The two symmetry operations for this point group are the identity operation E and the reflection operation σ_V, where σ_V is equivalent to AΓML plane. The order of the group is 2. The two, one dimensional, representations for this point group are either A_1 and A_2 or B_1 and B_2 in Γ-A-M plane so we simply labeled them as Γ_1 and Γ_2 species.

Table.4. 3. Character table of C_s point group.

C_s	E	σ_V
A_1	+1	+1
A_2	+1	- 1
B_1	+1	+1
B_2	+1	- 1

Now we will consider atomic displacement and behavior of modes in all four geometries with respect to phonon wave vector K_{phonon} in detail. Let us first consider the back scattering (BS) geometry from the surface (see fig4.5). As we already discussed that $K_{phonon} \parallel \Gamma$-A direction so phonon modes can be predicted by C_{6v} point group and the number of allowed Raman and IR modes are given by eq.4.13-4.14. In fig.4.6 the atomic displacement of atoms in unit cell of 4H-SiC in Γ-A direction is shown, simulated by computer aided lattice dynamic model (LDM) with important parameter, i.e. ionicity of 12% for SiC [17].

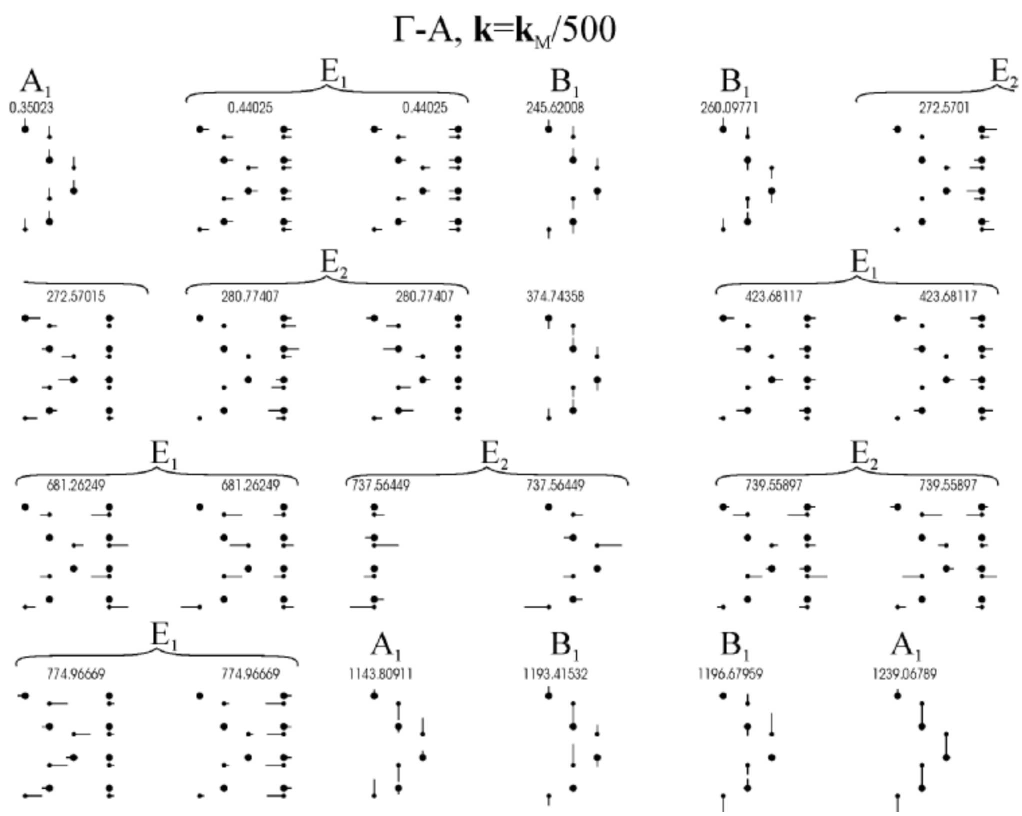

Fig.4.6 Atomic Displacement of atoms of 4H-SiC unit cell in Γ-A direction, simulated by Lattice Dynamic Model (LDM).

In this figure, atomic displacements corresponding to phonons of different energies are shown and labeled with the irreducible representations of C_{6v}, i.e. A_1, B_1, E_1 and E_2. We can observe from fig.4.6 that E modes are double degenerate. Each E mode has two atomic displacements in two directions because these are planar modes and it's not possible to show planar displacements only in the xoz or yoz plane. The first three modes in fig.4.6, i.e. A_1 at 0.35023 cm^{-1} and E_1 at 0.44025 cm^{-1} are acoustic modes and all the rest are optical modes. The B-modes are forbidden in Raman and IR spectroscopy. Hence the total number of observable modes is ten as given by eq.4.8.

The optical modes A_1 and E_1 are polar modes, which means that there exists an associated dipole moment and macroscopic electric field with these modes. E_2 modes are non-polar in nature. The strong polar modes are TO mode at 774 cm^{-1} and LO mode at 1239 cm^{-1} of symmetry E_1 and A_1 respectively. We can also see from fig.4.6 that for these modes i.e. E_1 (774 cm^{-1}) and A_1 (1239 cm^{-1}), the net dipole moment per unit cell is maximum, which implies that the net polarization also has non-zero value. Due to the non-zero polarization, the splitting is large for this E_1 (774 cm^{-1}) polar mode when the direction of the wave vector K_{phonon} with respect to c-axis changes. The A_1 mode does not split of course, but its energy also depends on the direction of K_{phonon}. Hence polar modes frequencies strongly depend upon the direction of the K_{phonon} due to the contribution of the macroscopic field.

For any scattering geometry we can classify the polar modes as longitudinal and transversal modes with respect to direction of K_{phonon} in BZ, as shown in our lattice dynamic calculation. The rest of the modes do not change significantly their atomic dispacement patterns therefore they remain purely axial or planar, see fig.4.8. Hence, the A_1 and B_1 modes remain longitudinal modes and E_1 and E_2 modes are transversal, also with respect to c-axis.

In back scattering geometry from edge K_{phonon} is parallel to Γ-M direction in BZ, i.e. perpendicular to c-axis of crystal and the modes are predicted by C_{2v} point group. The displacement of atoms in Γ-M direction in unit cell of 4H-SiC is simulated by LDM (see fig.4.7). If we compare fig.4.6 and fig.4.7 [17], we observe that E_1 modes split into B_1 and B_2 modes and E_2 modes decompose into A_1 and A_2 modes in back scattering geometry from edge. The acoustic modes are A_1 corresponding to 0.39074 cm^{-1}, B_1 corresponding to 0.30665 cm^{-1} and B_2 at 0.20083 cm^{-1} where B_1 and B_2 correspond to planar acoustic mode E_1. But these acoustic axial modes, B_1 and B_2, in C_{2v} symmetry are at higher energy than the planar acoustic E_1 in BS (surface).

In this geometry we can assign modes as longitudinal and transversal modes depending upon their direction with respect to K_{phonon}. For example the LO mode (A_1) at 1239 cm^{-1} in BS (surface) is shifted to wave number 767 cm^{-1} and in this scattering configuration it is TO mode (A_1) as atomic displacement are along y-axis. Similarly the TO mode E_1 at 774 cm^{-1} in BS (surface) geometry transformed into LO mode B_1 at 1243 cm^{-1} in BS (edge). One can see from fig.4.7, the strong polar modes are LO mode (B_1 at1243 cm^{-1}), and TO modes (A_1 at 767 cm^{-1}, B_2 at 774 cm^{-1}).

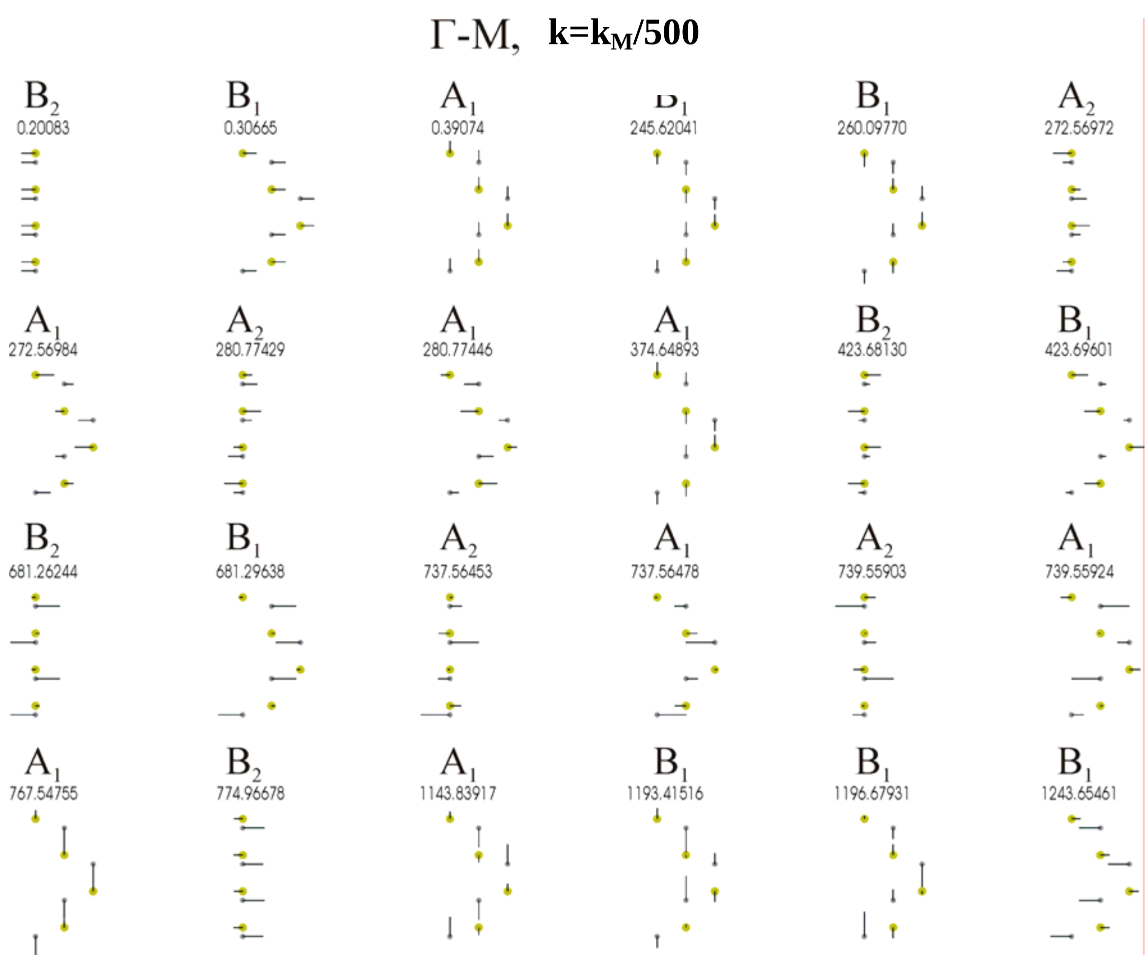

Fig.4.7. Atomic Displacement of atoms of 4H-SiC unit cell in Γ-M direction, simulated by Lattice Dynamic Model (LDM).

In rectangular geometries, the modes can be explained by the C_s point group. The character table of C_s point group is shown in table 4.3. In fig.4.8, the atomic displacement for 4H-SiC in Γ-A-M plane is shown [17]. The wave vector K_{phonon} is in xz plane at $\theta = 45^0$ with respect to c-axis. If we look at fig.4.8, the first three modes are acoustic while the rest are optical modes. The classification of modes as longitudinal and transverse modes is also with respect to direction of wave vector K_{phonon} in this geometry. We can observe that the strong polar mode (Γ_1 at 1241 cm^{-1}) is parallel to K_{phonon}, hence it can be classified as LO mode and the other two strong polar modes (Γ_1 at 771 cm^{-1} and Γ_2 at 774 cm^{-1}) are perpendicular to c- axis, so can be classified as TO modes. Thus indeed in all configurations the frequency of the polar LO mode is shifted up very sensibly by the association with it macroscopic electric field, as predicted by the theory.

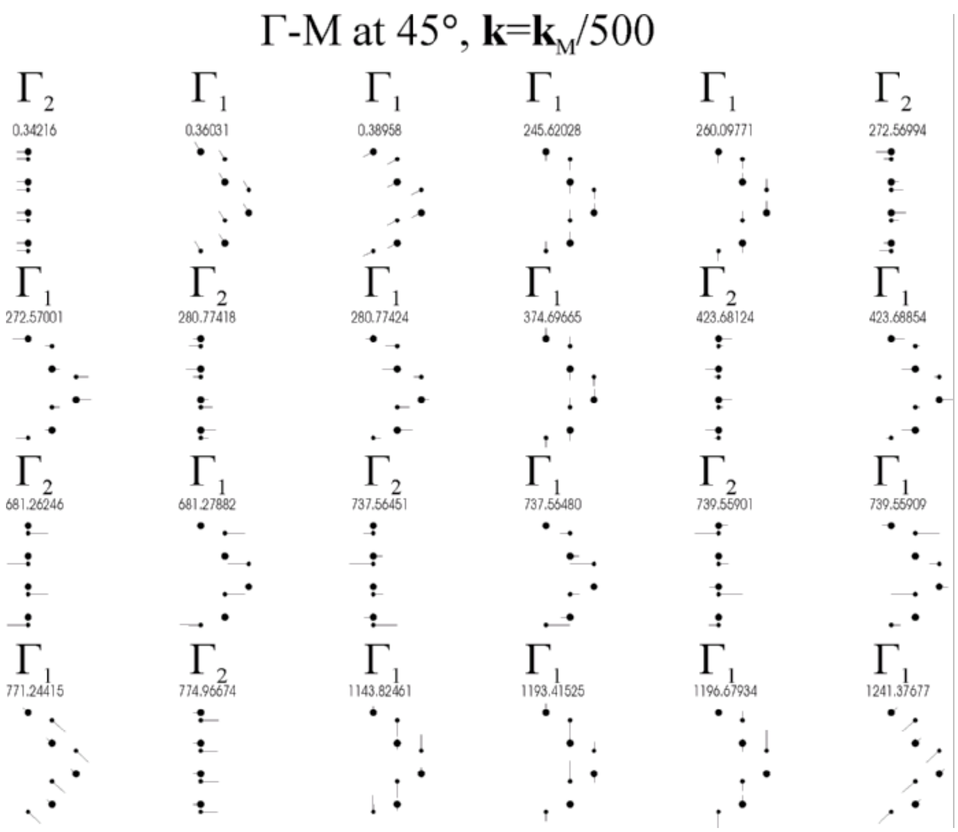

Fig.4.8. Atomic Displacement of atoms of 4H-SiC unit cell in Γ-A-M direction, simulated by Lattice Dynamic Model (LDM).

We have plotted the dependence of the energies of phonons near the Γ- point on the direction of the wave vector K_{phonon}, to investigate the angular dependence of phonons (fig 4.9). The angle $\theta = 0^0$, corresponds to K_{phonon} along Γ-A direction (BS from surface i.e. C_{6v} group) and the final angle $\theta = 90^0$ correspond to K_{phonon} along Γ-M direction (BS from edge i.e. C_{2v} group). The intermediate angles correspond to K_{phonon} in Γ-A-M plane (Rectangular geometry i.e. C_s group). If we observe the A_1 mode at 1239 cm^{-1} at $\theta = 0^0$ in fig.4.9, we can conclude that it has rather strong angular dependence and it has shift of ≈ 4 cm^{-1} at $\theta = 90^0$. Another important point is that this A_1 mode now has to be classified as B_1 mode of C_{2v} symmetry at $\theta = 90^0$, which confirms that K_{phonon} has different group in different directions of BZ for 4H and 6H-SiC. E_1 mode at 789 cm^{-1} at $\theta = 0^0$ also exhibit large energy shift ≈ 7 cm^{-1} at $\theta = 90^0$, which also confirm strong polar nature of this mode.

When we consider direction from Γ-A to Γ-M point, we can observe another point that splitting is large for polar A_1 and E_1 modes and E_2 modes have very negligible or no splitting at all. The scale in fig.4.9 is highly exaggerated around some energy in order to see the splitting of modes. This actually explains why the number of modes observed experimentally is less than the number of the theoretically predicted modes. The reason is that the splitting between modes is very small and it is hardly possible for even very good spectrometer to resolve this splitting.

Note that only one TO mode and one LO mode show significant angular (or directional) dependence, namely, the TO modes of E_1 symmetry with energies around 775 cm^{-1} and the highest energy LO mode of A_1 symmetry (at θ = 0°). On the other hand, all the modes of A_1 and E_1 symmetry are polar modes. However, the remaining polar modes are associated with vibrations stemming from the edge or other non-zero wave vector points of the large zones (Jones zone), i.e., they can be considered as appearing at the zone center due to the zone folding. Consequently, the displacements of the atoms are paired two by two for atoms of same species but with opposite signs, which leads to near cancellation of the polarization contributed by the unit cell.

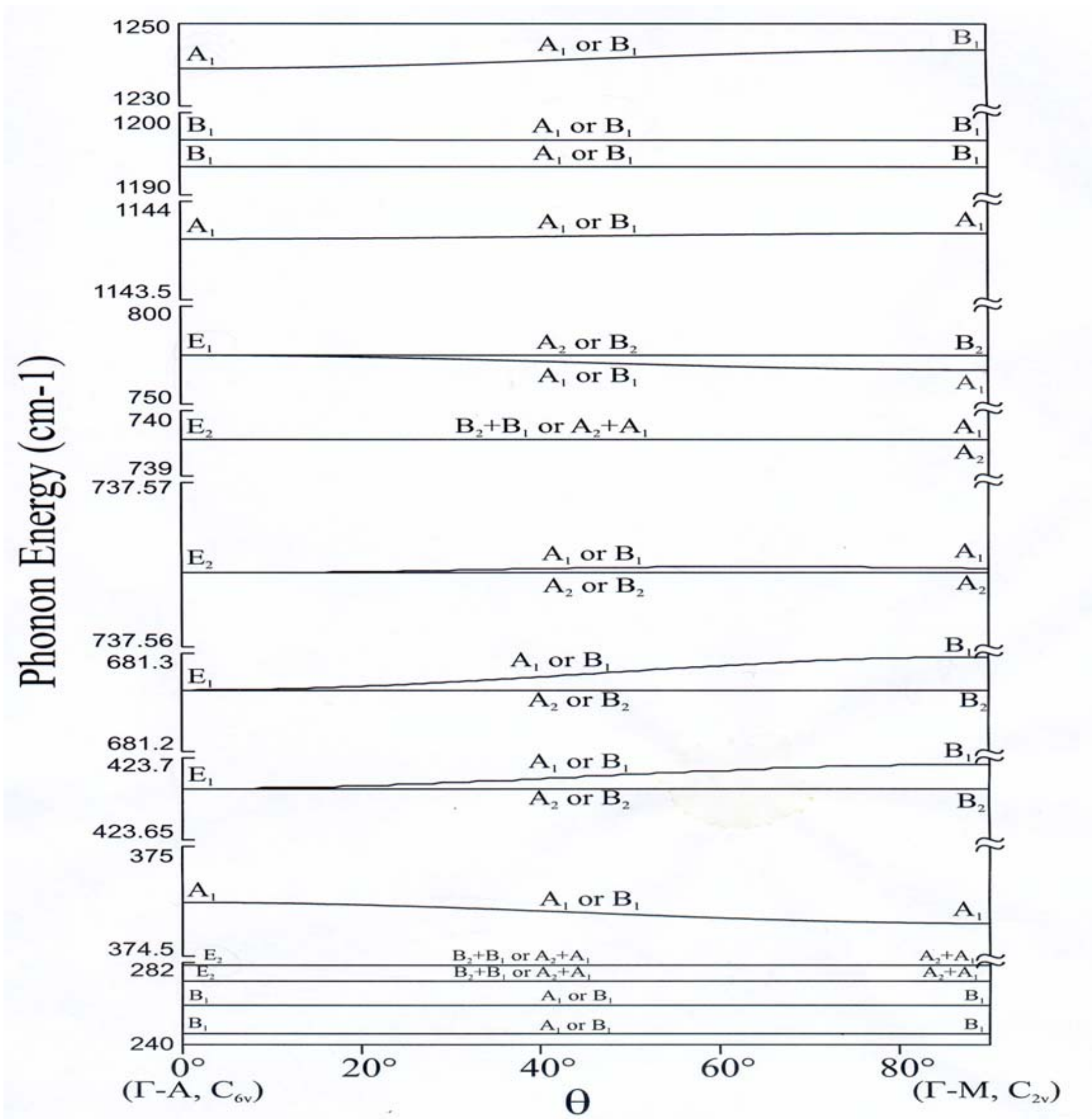

Fig.4.9. Angular dependence of the phonon energies of the optical phonons in 4H-SiC calculated with a lattice dynamical model. θ is the angle between the Γ-A direction of the Brillouin zone (BZ) and the phonon wave vector. The amplitude of the latter is constant chosen to be 1/500 of the extension of the BZ in the Γ-M direction. Note the breaks on the energy axis and the very different energy scales for the different phonon branches chosen so as to make visible all the splittings of the branches with E_1 symmetry (and also of one branch of E_2 symmetry). The classification of the phonons by symmetry is done within C_{6v} at θ = 0° (Γ-A direction), C_{2v} at θ = 90° (Γ-M direction), and C_s for arbitrary θ between these limits, because these are the groups of the wave vector for the corresponding directions

Only the original (not folded) modes, which are common for all polytypes, contribute strongly to the polarization of the unit cell, because the four (in the case of 4H-SiC) atoms of each species vibrate in phase, creating vibration of the silicon and carbon sublattices against each other. This yields the maximum possible value for the polarization of one unit cell. This is illustrated very well by the displacements patterns of the atoms presented in Fig. 4.6 and Fig.4.7 for the cases of the phonon wavevector along the Γ-A and Γ-M directions, respectively. Note that the places of one of the polar transversal modes and the longitudinal polar mode with highest energy are interchanged. This is easily understandable in view of the fact that the phonon wave vector has different direction for these two figures, the important issue being that the polar modes (but not any other mode) can be classified as longitudinal and transversal *with respect to the direction of the wave vector* for arbitrary direction of the latter.

Table.4.4. Compatibility table for phonon modes in different direction of BZ.

C_{6v}	**A_1**	**A_2**	**B_1**	**B_2**	**E_1**	**E_2**
C_{2v}	**A_1**	**A_2**	**B_1**	**B_2**	**$B_1 + B_2$**	**$A_1 + A_2$**
C_s	**Γ_1**	**Γ_2**	**Γ_1**	**Γ_2**	**$\Gamma_1 + \Gamma_2$**	**$\Gamma_1 + \Gamma_2$**

Hence we found out that the polar modes have very strong dependence on the direction of wave vector K_{phonon} and the phonons have totally different symmetry and character in different geometries as well as there is large splitting and energy shift for polar modes. So here we can formulate a compatibility table, which can explain the transformation of phonon in different symmetry point group. The theoretical analysis for 6H-SiC can be done in similar way and the modes in 6H will follow the same behavior as in 4H-SiC. The only difference is that it has larger number of modes as it has 12 atoms per unit cell. Table.4.4 gives the compatibility relations of phonon modes in three point groups i.e. C_{6v}, C_{2v} and C_s, which correspond to three different directions of K_{phonon} in BZ.

4.2. Classification of Phonons with respect to Polarization Vectors of Incident and Scattered Raman light.

As we discussed before that the mode symmetry and appearance depends on many factors, especially on the direction of the wave vector K_{phonon}. The sample geometry measured is also very important to be considered to study the symmetry of phonons. The prediction of intensity I(k) of each mode can be made theoretically using the simple relation, i.e.,

$$I(k) = (e_s \chi_k e_i)^2 \quad \textbf{(4.16)}$$

where e_i and e_s are the polarization vectors of incident and scattered light and χ_k is the Raman tensor and has different form for modes of different symmetry. The form of the Raman tensor for back scattering (surface) geometry, which correspond to C_{6v} group, are given below:

$$\chi_{A_1} = \begin{pmatrix} a & 0 & 0 \\ 0 & a & 0 \\ 0 & 0 & b \end{pmatrix}, \quad \chi_{E_1,x} = \begin{pmatrix} 0 & 0 & c \\ 0 & 0 & 0 \\ c & 0 & 0 \end{pmatrix}, \quad \chi_{E_1,y} = \begin{pmatrix} 0 & 0 & 0 \\ 0 & 0 & d \\ 0 & d & 0 \end{pmatrix}$$

$$\chi_{E_2,1} = \begin{pmatrix} e & 0 & 0 \\ 0 & e & 0 \\ 0 & 0 & 0 \end{pmatrix}, \chi_{E_2,2} = \begin{pmatrix} 0 & f & 0 \\ f & 0 & 0 \\ 0 & 0 & 0 \end{pmatrix}$$

Note that the two tensors χ_{E_1} and χ_{E_2} correspond to each of the two-dimensional representation.

The polarization vectors can have four different forms for BS (surface) geometry i.e. $z(xx)\bar{z}, z(xy)\bar{z}, z(yx)\bar{z}, z(yy)\bar{z}$, where z and $\bar{z}$ represents the direction of wave vector k for incident and scattered light respectively and alphabets in bracket represent the polarization vector e_i and e_s for incident and scattered light respectively for all four cases of BS (surface) geometry. We did calculations, using eq.4.16 to see which mode is appearing with strong or weak intensity for all the four cases (mentioned in above lines) of BS (surface) geometry. We can compare the intensity of modes obtained theoretically and experimentally and this will help us to identify the modes in our experimental spectra.

Here is an example to understand how triple product from eq.4.16 can be calculated. For example, for $z(xx)\bar{z}$ case of BS (surface) geometry, the polarization vector, e_i for incident laser light and e_s for scattered light has the form given in eq.4.18.

$$e_s = \begin{pmatrix} 1 & 0 & 0 \end{pmatrix}, e_i = \begin{pmatrix} 1 \\ 0 \\ 0 \end{pmatrix} \qquad \textbf{(4.17)}$$

Solving eq.4.16 for the polarization vectors given in eq.4.17, we found out that for scattering configuration $z(xx)\bar{z}$, the Raman lines of axial $A_1$and planar E_1 and E_2 species can be observed proportional to a^2, d^2 and we found that E_1 modes are not allowed in this geometry.

Table.4.5.1. Theoretical prediction of modes for BS (Surface) geometry calculated by eq4.17.

Back scattering (Surface)	$z(xx)\bar{z}$	$z(xy)\bar{z}$	$z(yx)\bar{z}$	$z(yy)\bar{z}$
A_1	**a^2**	**0**	**0**	**b^2**
E_1	**0**	**0**	**0**	**0**
E_2	**e^2**	**f^2**	**f^2**	**e^2**

Similarly we did calculation for the other three BS (surface) configurations and results are summarized in table.4.5.1. We also observed that in the BS (surface) geometry, the A_1 modes are polarized parallel to the polarization of laser light, the E_1 modes are forbidden in this geometry for all configurations and the E_2 modes are also polarized both in the direction of polarization of incident light and perpendicular to it, i.e., they are depolarized.

In the BS (edge) geometry, the Raman tensors for the modes are given below for C_{2v} symmetry group. The component to which intensity of species is proportional, is calculated using eq.4.17 for the four BS (edge) configuration i.e. $x(zz)\bar{x}, x(zy)\bar{x}, x(yz)\bar{x}, x(yy)\bar{x}$. The A_1 species appear only when the scattered intensity is polarized along the polarization direction of incident light, A_2 and B_1 modes are forbidden in this geometry, while the B_2 modes appear only when the polarization vector of scattered light is perpendicular to polarization vector of incident light.

$$A_1 = \begin{pmatrix} a & 0 & 0 \\ 0 & b & 0 \\ 0 & 0 & c \end{pmatrix}, A_2 = \begin{pmatrix} 0 & d & 0 \\ d & 0 & 0 \\ 0 & 0 & 0 \end{pmatrix},$$

$$B_1 = \begin{pmatrix} 0 & 0 & e \\ 0 & 0 & 0 \\ e & 0 & 0 \end{pmatrix}, B_2 = \begin{pmatrix} 0 & 0 & 0 \\ 0 & 0 & f \\ 0 & f & 0 \end{pmatrix}$$

In addition, we can say about these modes is that the A_1 modes are polarized parallel to c-axis of crystal in $x(zz)\bar{x}$ scattering configuration, and perpendicular to c-axis in $x(yy)\bar{x}$ scattering configuration. The results are summarized in table.4.5.2.

Table.4.5.2. Theoretical prediction of modes for BS (Edge) geometry calculated by eq4.17.

Back scattering (Edge)	$x(zz)\bar{x}$	$x(zy)\bar{x}$	$x(yz)\bar{x}$	$x(yy)\bar{x}$
A_1	**c^2**	**0**	**0**	**b^2**
A_2	**0**	**0**	**0**	**0**
B_1	**0**	**0**	**0**	**0**
B_2	**0**	**f^2**	**f^2**	**0**

Cs group gives the mode symmetry in rectangular geometries. Hence the Raman tensors for C_s groups are given below.

$$\Gamma_1 = \begin{pmatrix} a & d & 0 \\ d & b & 0 \\ 0 & 0 & 0 \end{pmatrix}, \Gamma_2 = \begin{pmatrix} 0 & 0 & e \\ 0 & 0 & f \\ e & f & 0 \end{pmatrix}$$

The four scattering configuration for rectangular geometry (E_L through surface, E_r through edge) are $z(xz)x, z(xy)x, z(yz)x, z(yy)x$ while for the other rectangular geometry (E_L through edge, E_r through surface), the four scattering configurations are $x(zx)z, x(zy)z, z(yx)z, x(yy)z$. By using eq.4.17 for different scattering configurations for both the geometries, we found out that these two are equivalent geometries. Both Γ_1

and Γ_2 modes are allowed in these geometries in certain configurations. The summary of results is given in the table.4.5.3.

Table.4.5.3. Theoretical prediction of modes for Rectangular geometry calculated by eq.4.17.

Rectangular Geometry(E_L via surface)	$z(xz)x$	$z(xy)x$	$z(yz)x$	$z(yy)x$
Γ_1	**0**	e^2	**0**	b^2
Γ_2	f^2	**0**	i^2	**0**
Rectangular Geometry(E_L via edge)	$x(zx)z$	$x(zy)z$	$x(yx)z$	$x(yy)z$
Γ_1	**0**	**0**	d^2	b^2
Γ_2	f^2	**0**	i^2	**0**

After all this discussion, we should keep this in mind that the C_2 and C_s are low symmetry group for these geometric configurations so the polarization vectors should be compatible to our geometries in this case. Hence it might be possible that in geometries which are govern by C_2 and C_s point groups, the modes, which are not predicted theoretically, can be observed experimentally. But it should not be confused with wave vector K_{phonon}, as C_2 and C_s are group of the wave vector K_{phonon} in different directions of the BZ of crystal.

4.3. Experimental Details and Interpretation of Observed phonons

In this section we will compare the experimental results of Raman and Infrared absorption of 4H-SiC with the theoretical results and provide an overview of the results for 6H-SiC. We also tried to assign the representations to these Raman and infrared absorption lines based on the theoretical knowledge but this assignment for some of the lines has to be considered as tentative, before a more detailed theory giving explicit expressions for the Raman tensors in various symmetries is built. Such a theory is now in process of development.

For the Raman measurements we used 4H and 6H-SiC samples of thickness ~ 55 μm with c-axis nearly perpendicular to the surface (8^0 off). All the measurements were done at room temperature. The excitation source used is Argon laser, which is tunable to different discrete wavelengths. The laser wavelength we used is 458nm. This laser wavelength is well below the electronic band gap of SiC and the material is transparent for it ensuring good signal to noise ratio. Some researchers have used higher wavelength like 514 nm but we did not use it just because photomultiplier of Raman setup has better sensitivity at shorter wavelengths. Raman spectra measured were averaged over 10-20 scans with integration time of one second. It is always better to have small integration time with large number of scans than a single scan with long integration time because any spike can be averaged out easily. Similarly set up can have some minute vibrations so it is always good idea to have more scans with small integration time.

We will first discuss the most common back scattering geometry (surface), see fig.4.10, which correspond to C_{6v} group of wave vector K_{phonon}. Although the total number of the Raman modes predicted theoretically are ten (eq.4.8), the total number of the Raman lines appearing are roughly seven in all spectra of the scattering configurations of the back scattering (surface) geometry. The reason behind this can be that it is difficult to resolve the modes close in the energy even with a very good spectrometer. If we consider fig.4.4 in detail, we can observe an interesting feature. The dispersion curves of the three polytypes displayed in the fig.4.4 has about the same energy gap between acoustic and optical modes, ranging from ~ 610 cm^{-1} to 730 cm^{-1}.

Our theoretical prediction, (see fig.4.9), underestimates the energy gap, i.e., from ~ 400 cm^{-1} to 650 cm^{-1}. The reason is that we use the non-modified force constant as given by the Tersoff [19]. The adjustment of force constant may provide a better fit to the experimental energies and may lead also to re-ordering of the states. Therefore, we will discuss only model-independent theoretical features such as the existence of energy and the number of phonons above and below it. There are two, i.e. LO and TO, modes above the energy gap, and two, i.e. TA and LA, modes below this energy gap in the basic BZ of

3C-SiC. Hence from fig.4.9, we can say that 4H-SiC has five optical modes, i.e. $2A_1+2E_1+2E_2$ above the energy gap and four optical modes, i.e. $1A_1+1E_1+2E_2$, below it. This classification of the modes below and above the band gap will be very useful to label the Raman lines with the specific representation

The Raman line at 966 cm^{-1} is the high energy LO mode (as LO modes are always at higher energies) and it is assigned as A_1 species in the fig.4.6. (However the energy given in fig.4.6 does not match the experimental one as explained above). Therefore the Raman line at 966 cm^{-1} can be labeled as A_1 and later we will justify our assignment when we will analyze the experimental results for other geometries. For the moment, we assign the Raman line at 799 cm^{-1} as E_1, the line at 778 cm^{-1} and shoulder at 785 cm^{-1} as the E_2 modes. Here we can question the appearance of the E_1 mode at 799 cm^{-1}, as it is not allowed in the BS (surface) geometry (see table 4.5.1). The appearance of E_1 mode in this geometry is most probably due to imperfect geometry. There should be another A_1 mode above the energy gap according to our above classification but it might be overlapping one of the strong lines. By imperfect geometry we mean that the orientations of geometry in the measurement are not as accurate as shown in fig.4.5.

Below the energy gap, we should assign the 610 cm^{-1} line as E_1 mode according to our theoretical result given in fig.4.9, (as it is just below the energy gap). But it is also observed that when we use the different ionicity parameter in our LDM model, the ordering of modes as shown in fig.4.9 and fig.4.6 is different and the mode just below the band gap is A_1 instead of E_1. Similar reordering of the states is expected with changing the short-range force constants in our LDM, as explained before. Therefore, we will base our assignment on the intensity behavior of the line in different scattering geometries rather than on the ordering of the states predicted by the model. We note, however, that ionicity of 12% (as used in the model in agreement with previous work [17]) correctly predicts the shift of the polar LO mode and the splitting of the polar TO mode in different geometries, as will be seen. This is so because the shift and the splitting mentioned above are entirely due to the long-range coulomb interactions between the ions, which in term is determined by a single parameter, the effective charge of the positive/negative ion (Si and

C, respectively). The Raman lines at 194 cm^{-1} and at 204 cm^{-1} are assigned as the E_2 modes and line at 266 cm^{-1} as the E_1 mode. We will observe the behavior of these modes in other geometries and try to justify this assignment of Raman lines.

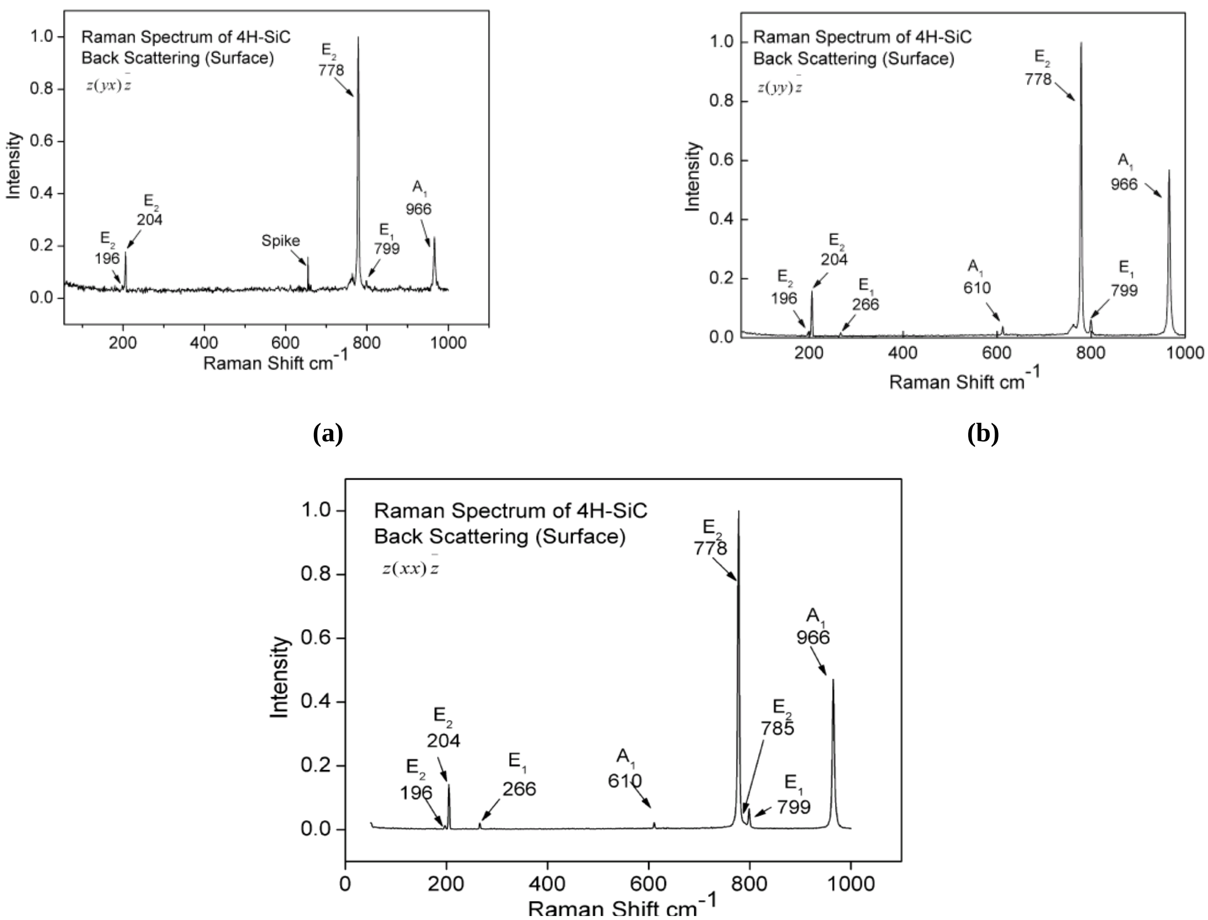

(a) **(b)**

(c)

Fig.4.10. Raman Spectra of 4H-SiC for back scattering (surface) geometry, where a) represents $z(yy)\bar{z}$ configuration and b) represents $z(yx)\bar{z}$ configuration and c) represents $z(xx)\bar{z}$ configuration.

Back scattering from the edge is another measurement geometry, which reveals important results. As we know the group of the wave vector K_{phonon} is C_{2v} in this case but here we should understand that it is the local symmetry group of crystal and C_{6v} represent the real symmetry point group of the crystal. The Raman spectra for all four configurations of back scattering configuration (edge) for 4H-SiC are shown in fig.4.11. The Raman lines appearing in this geometry are not more than nine even though the theoretically predicted number of lines is twenty-one. As we know that in C_{2v} group, all the representations are one-dimensional but we will label the modes using the notations of the irreducible representations of C_{6v} in order to show from which mode, originates one or more Raman line.

The 971 cm^{-1} Raman line is the polar LO mode and can be labeled then as A_1 mode. This mode has energy shift of ~ 4 cm^{-1} in this geometry, which is consistent with our theoretical results given in fig.4.9. Hence it confirms that this is the longitudinal axial mode (LA). There is another new mode at 839 cm^{-1}, which does not appeared in BS (surface) geometry. We can assign this 839 cm^{-1} line as E_1 mode because these (E_1) modes are not allowed in BS (surface) geometry according to our theoretical results (see table.4.5.1). If we compare the intensity of 266 cm^{-1} line in both BS (surface) and BS (edge) geometries, this mode is also a good candidate for E_1 mode as it is also significantly enhanced in BS (edge) geometry.

According to theory, this E_1 (266 cm^{-1}) mode must also exhibit splitting in this geometry but it is not observable because this splitting is very small to be resolved, i.e. of the order of 0.014 cm^{-1} according to our model (fig.4.9). The E_1 mode at 799 cm^{-1} split into B_2 and B_1 mode but as B_1 mode are not allowed in this geometry (see table.4.5.2) we cannot observe this counterpart.

If we compare all the four scattering configurations for BS (edge) geometry, we can see that the A_1 mode at 971 cm^{-1} is stronger in all configurations except the $x(yy)\bar{x}$ configuration, which is not consistent with our result given in table.4.5.2. The one reason can be that as we said that the C_{2v} is just local group for our crystal system and the forms of Raman tensor for C_{2v} used for theoretical treatment is not fully compatible with our crystal system and a more detailed microscopic theory is needed. The E_1 mode at 799 cm^{-1} (splits into B_1+B_2 at $\theta = 90^0$) is more intense in $x(zy)\bar{x}$ and $x(yz)\bar{x}$ and it is consistent with our theoretical results. The E_2 mode at 785 $cm^{-1}$is very strong in all geometry and even stronger than the E_2 mode at 778 cm^{-1} in the $x(zz)\bar{x}$ configuration. All the other modes are consistent with theoretical results summarized in table.4.5.2 for this geometry. We can also observe that the $x(zy)\bar{x}$ and $x(yz)\bar{x}$ configurations are equivalent (see fig.4.11)

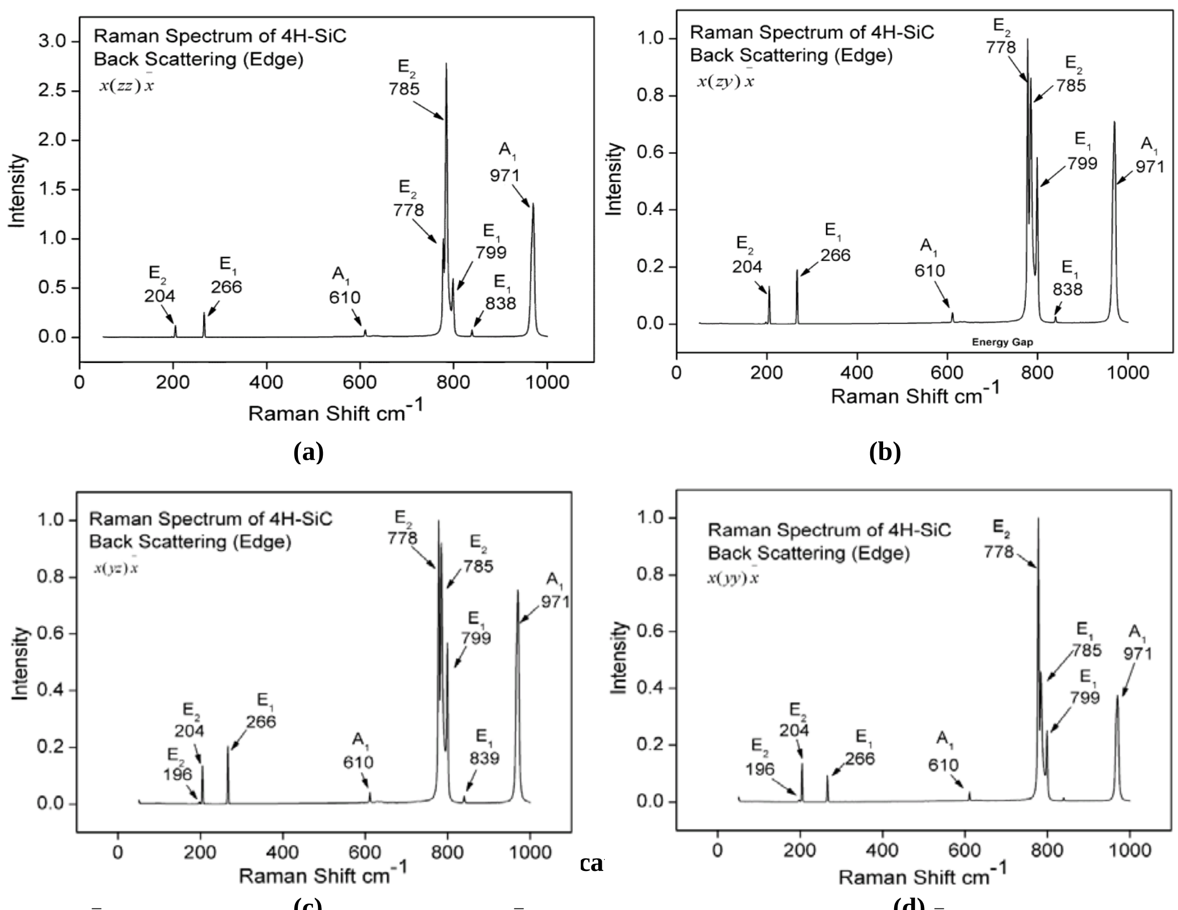

ca

$x(zz)\bar{x}$ **configuration, b) represents** $x(zy)\bar{x}$ **configuration, c) represents** $x(yz)\bar{x}$ **configuration and d) represents** $x(yy)\bar{x}$ **configuration.**

The Raman spectra of 4H-SiC for the four configurations of rectangular geometry are shown in fig.4.12 and fig.4.13. Two of the rectangular geometries are equivalent according to our theoretical results. Now we will study the experimental spectra and compare them to our theoretical results. As we know the group of K_{phonon} is C_s for rectangular geometry and all representations are allowed in Raman and can correspond to A_1 and A_2 or B_1 and B_2.

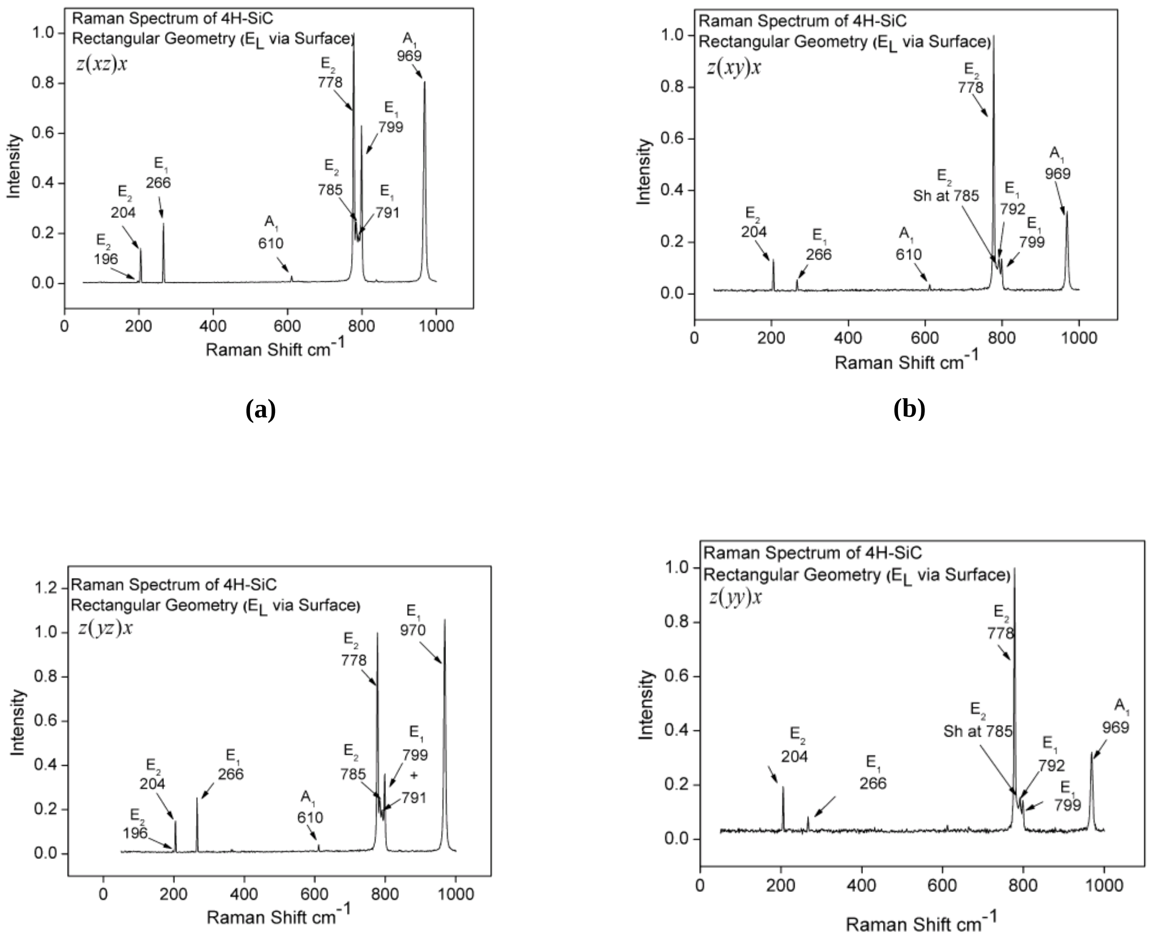

(c) (d)

Fig.4.12. Raman Spectra of 4H-SiC for rectangular scattering (excited via surface) geometry, where a) represents $z(yz)x$ configuration, b) represents $z(yy)x$ configuration, c) represents $z(xz)x$ configuration, d) represents $z(xy)x$ configuration.

We will consider first the rectangular geometry for which we excite through surface and receive through edge (see fig.4.12). The LO mode, A_1, is shifted to 969 cm^{-1} except for the z(yz)x configuration. The E_1 mode at 799 cm^{-1} splits into B_1 and B_2 or more generally speaking into Γ_1 and Γ_2. This particular mode split into B_1 and B_2, where B_2 has no shift and it appears at 799 cm^{-1} but the B_1 mode at 791 cm^{-1} exhibits a large energy shift of ~ 8cm^{-1} towards lower wavenumbers.This energy shift of the B_1 mode is also predicted theoretically (see fig.4.9), hence it suggests that the assigned representation for this doublet (corresponding to E_1 mode at 799 cm^{-1} in back scattering geometry from surface) is correct. We can see the splitting of this mode, since both B_1 and B_2 modes are allowed in this geometry. Another important feature to note about the E_2 mode at 785 cm^{-1} is that it is significantly weaker in nearly all configurations of this geometry

The other case of rectangular geometry measured experimentally is when we excite the sample through the edge and received from the surface (see fig.4.13). The LO mode appeared at 971 cm^{-1} while this mode in later case of rectangular geometry has energy shifted to 969 cm^{-1} in x(yz)z and x(yy)z, while in x(zx)y and x(zy)y configurations it is shifted to 971 cm^{-1}. The E_1 mode at 839 cm^{-1} appeared only in x(zx)y and x(zy)y but disappeared in the other two configurations, i.e. x(yz)z and x(yy)z. The E_2 mode at 785 cm^{-1} is quite dominant in all the configurations for this case of rectangular geometry, which was not the case for rectangular geometry with excitation through the surface. The E_2 mode at 196 cm^{-1} is also present (but weak) in all configurations. This mode also appeared in all the configurations of the rectangular geometry when we excite through surface except the z(yy)x configuration. The 778 cm^{-1} mode is strong in all configurations for both cases of the rectangular geometry.

If we compare the two geometries, we found that the z(yy)x (fig.4.12) is equivalent to x(yy)z (fig.4.13). Similarly the z(xy)x is equivalent to x(yx)z configuration. The z(yz)x and x(zy)z configurations are non-equivalent because the mode at 839 cm^{-1} disappeared in z(yz)x configuration and there is large difference of intensity for the mode at 785 cm^{-1}. Similarly, the two configurations x(zx)z and z(xz)x are also non-equivalent (see fig.4.12 & fig.4.13). Thus a more advance model is required to explain these observations.

Now we will discuss the IR absorption result obtained experimentally for 4H-SiC. For 4H polytype, we used two kinds of samples; one was bulk material of thickness 0.359mm, and the other sample of 4H was free-standing epitaxial layer of thickness 55μm. For both samples the c-axis was roughly perpendicular (8^0 off) to the sample surface. For the 6H polytype we used two samples; one was bulk of thickness 3.031 mm with c-axis cut and polished parallel to the c-axis. The other sample was free-standing epi layer of thickness 55μm and with the c-axis nearly perpendicular (3.5^0 off) to the plane. These epitaxial samples had negligible background doping of nitrogen. Note that the thickness of samples used for IR absorption measurement unlike Raman has to be chosen appropriately for transmission measurements.

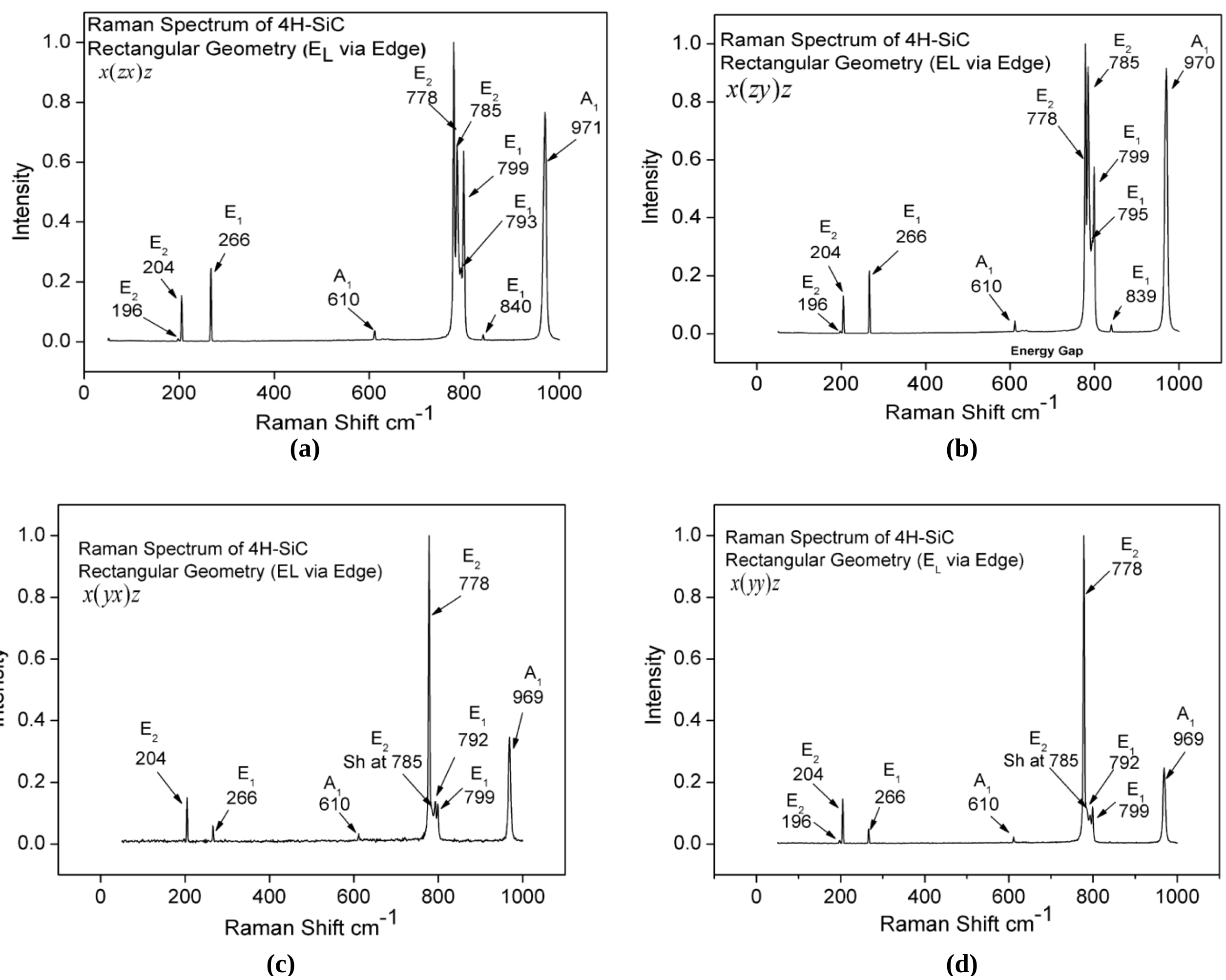

Fig.4.13. Raman Spectra of 4H-SiC for Rectangular (excited via Edge) geometry, where a) represents $x(zx)z$ configuration, b) represents $x(zy)z$ configuration, c) represents $x(yx)z$ configuration and d) represents $x(yy)z$ configuration.

The infrared transmission measurements were performed on a 'Biorad Fourier Transform Infrared Spectrometer', KBr Beam splitter and a DTGS (dueterated triglycine sulphate) detector. Measurements were taken at room temperature with beam incident at angle of 30^o, 0.5 cm^{-1} resolution and averaged over 1000 scans. The source used for IR light was ordinary lamp. Reference spectra for transmission measurements were recorded without any sample. The IR absorption spectra for 4H-SiC, bulk and epi sample are shown in fig 4.15a and 4.15b respectively. There is only one geometry measured for IR transmission measurements, as it was not possible to change the setup's settings. The geometry measured is shown in fig.4.14.

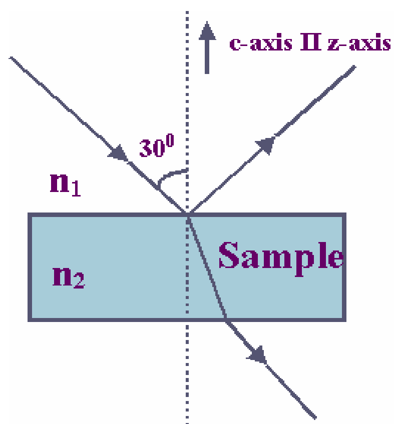

Fig.4.14. Sample geometry measured in IR experiment. The beam is incident on sample surface at a 30^0 angle. n_1 and n_2 is refractive index of air and sample respectively. The c-axis is polished perpendicular to surface and is taken along z-axis of crystal.

In fig.4.15a (transmission measurements of the 4H bulk sample), we can see the line at $610cm^{-1,}$ which is the characteristic axial mode, A_1, according to our assignment of modes in Raman spectra. This mode is also reported in Raman scattering experiments. This line disappears in sample with polarization of light perpendicular to c-axis of crystal, i.e. E⊥c but it appears in our measurements because our samples (bulk and epi4H-SiC) were cut and polished with c-axis orthogonal but 8^0 off and moreover the incident beam has incidence angle of 30^0. The Restrahlen band region ranges from w_{TO}=$765cm^{-1}$ to

w_{LO}=970cm^{-1}. There is a hump around 800cm^{-1}in the high reflectivity region, which is also reported in 6H [20]. The origin for this hump is unknown however it possibly has extrinsic nature.

In fig 4.15b (Transmission measurements of the 4H epi sample) strong line at 610cm^{-1}and a line at 738cm^{-1} also appeared. The line at 738cm^{-1} appears in sample with both polarizations; $E \parallel c$ and $E \perp c$, and is also reported in 6H-SiC [22]. Line with very weak intensity at 747cm^{-1} is also observed which is characteristic for a measurement with polarization in direction parallel to c; $E \parallel c$ but we observed it in our measurement due to not perfectly orthogonal orientation of c-axis with respect to planes. The 738cm^{-1}and 747cm^{-1} lines cannot be seen in the 4H bulk sample due to large thickness. Restrahlen region lies between w_{TO}=765cm $^{-1}$ and w_{LO} =970 cm^{-1}.

In the IR spectra of the epitaxial free-standing layer(see fig.4.15a-b) we can see interference fringes. These fringes are due to interference of the light reflected from the top surface of the sample with the light reflected from the bottom one and can be used to calculate the thickness of samples.

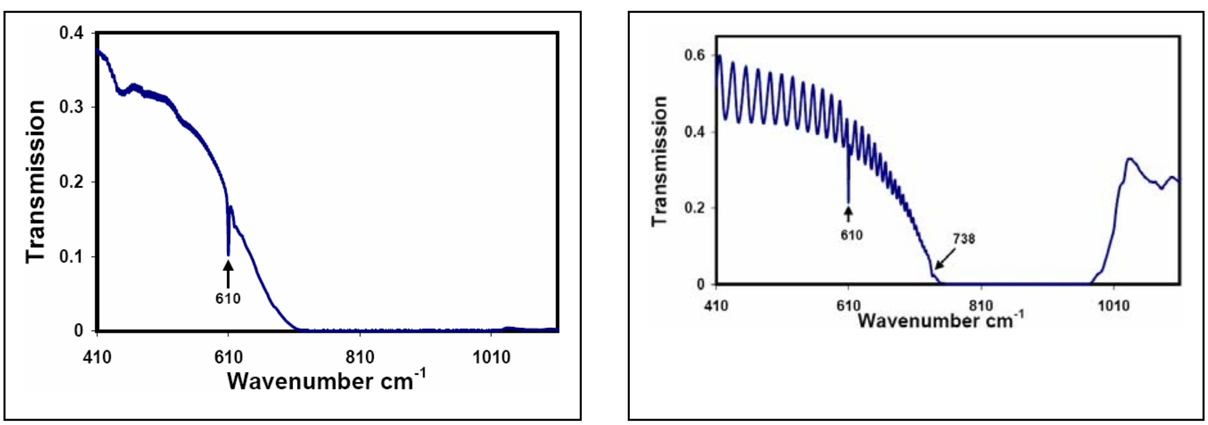

(a) **(b)**

Fig.4.15a. IR-absorption Spectrum for bulk 4H- SiC, b) IR-absorption spectrum for free standing epi sample (4H-SiC)

The relation to find thickness (at normal incidence) is

$$d = \frac{1}{2n(k_1 - k_2)} \qquad \textbf{(4.18)}$$

where $k_1=1/\lambda_1$ and $k_2=1/\lambda_2$ are wavenumbers according to the wavelengths of two subsequent fringes, and n is the refractive index in the region of these wavelengths.

The IR and Raman spectra of 6H-SiC are also shown in fig.4.16 – fig.4.20. These spectra are not discussed in detail but the analysis of these spectra is quite similar to 4H-SiC spectra and same theoretical arguments can be used to label the Raman lines though 6H-SiC has its own characteristic phonon modes. Due to the larger number of modes in 6H-SiC, an adequate model of the susceptibility is necessary for unambiguous identification of the phonon symmetries.

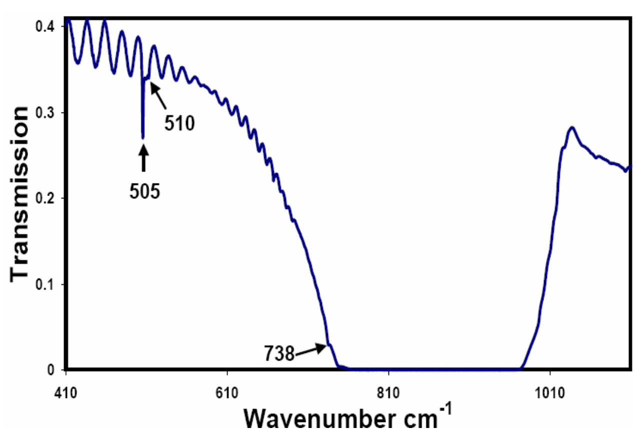

Fig.4.16. IR-absorption spectrum for free standing epi sample (6H-SiC). We were not able to observe transmission spectra of bulk sample of 6H-SiC due to large thickness of bulk sample,

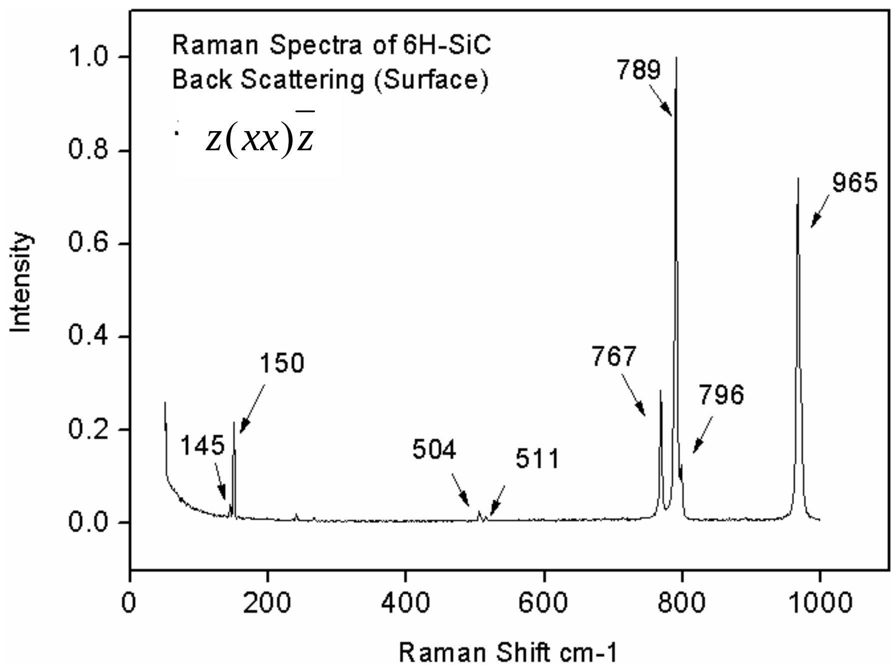

(a)

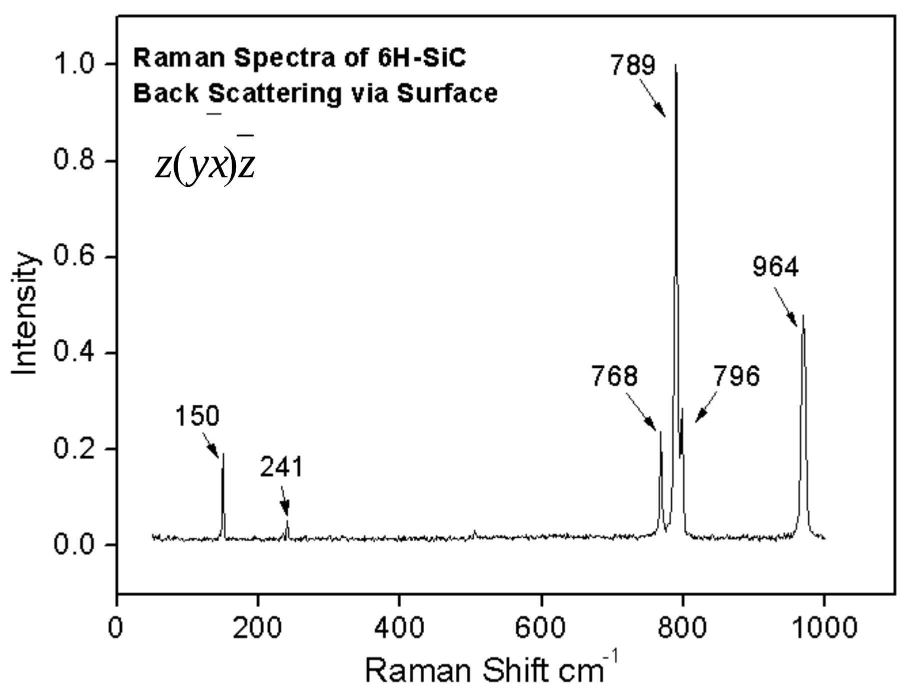

(b)

Fig.4.17. Raman Spectra of 6H-SiC for back scattering (surface) geometry, where a) represents $z(xx)\bar{z}$ configuration and b) represents $z(yx)\bar{z}$ configuration.

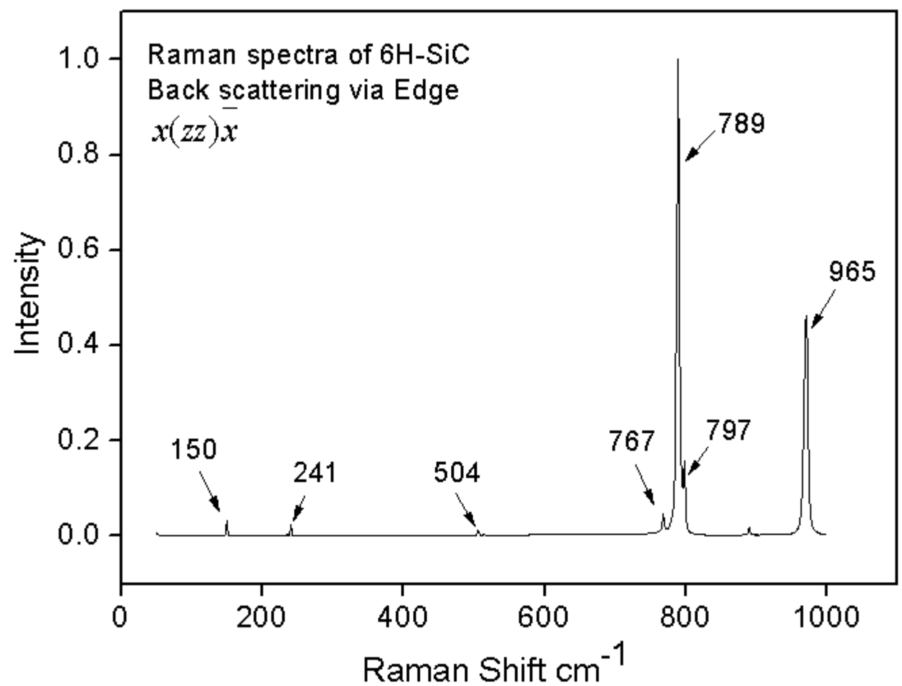

(a)

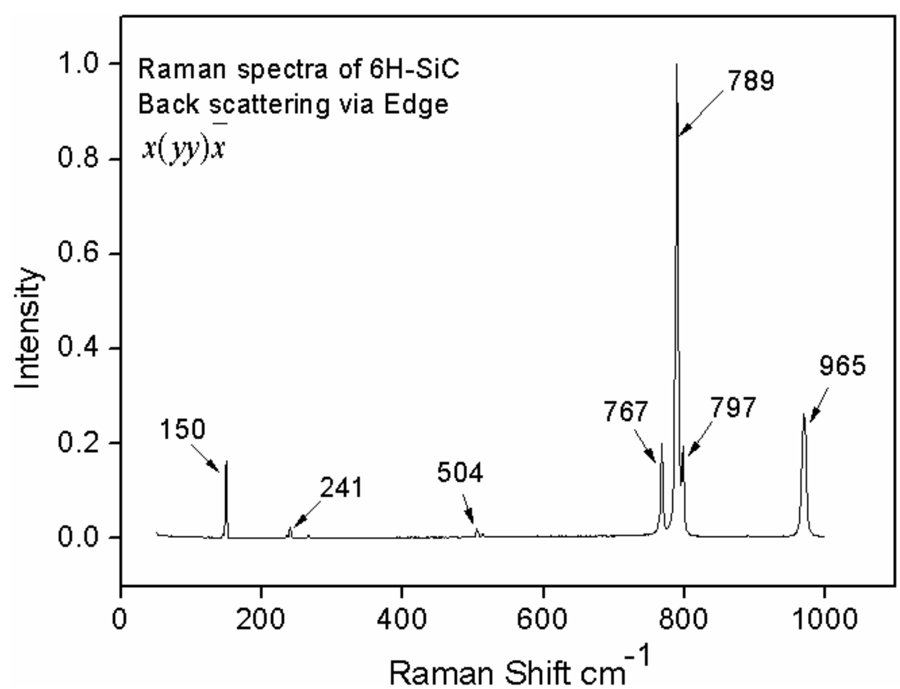

(b)

Fig.4.18. Raman Spectra of 6H-SiC for back scattering (edge) geometry, where a) represents $z(xx)\bar{z}$ configuration and b) represents $z(yx)\bar{z}$ configuration.

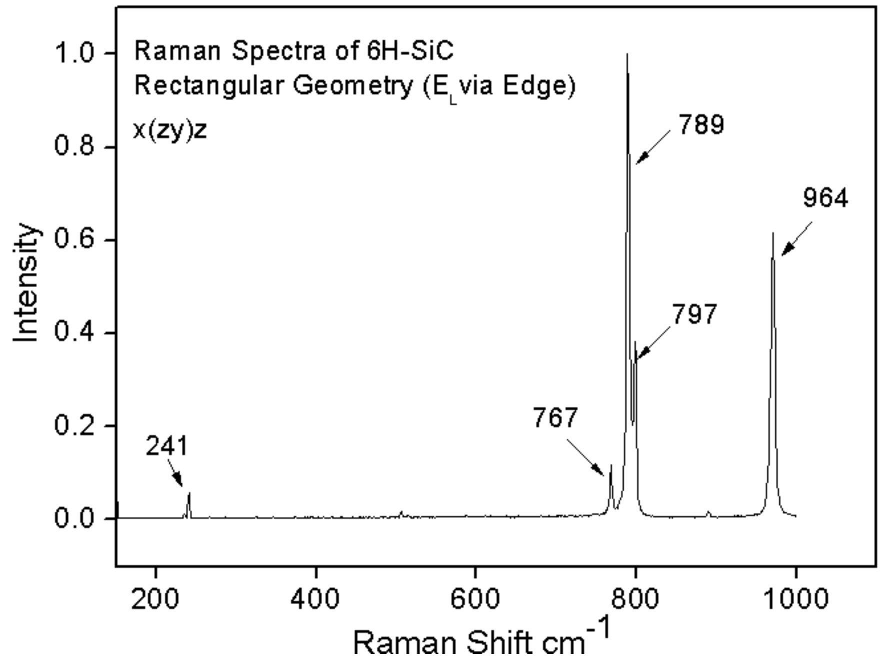

(a)

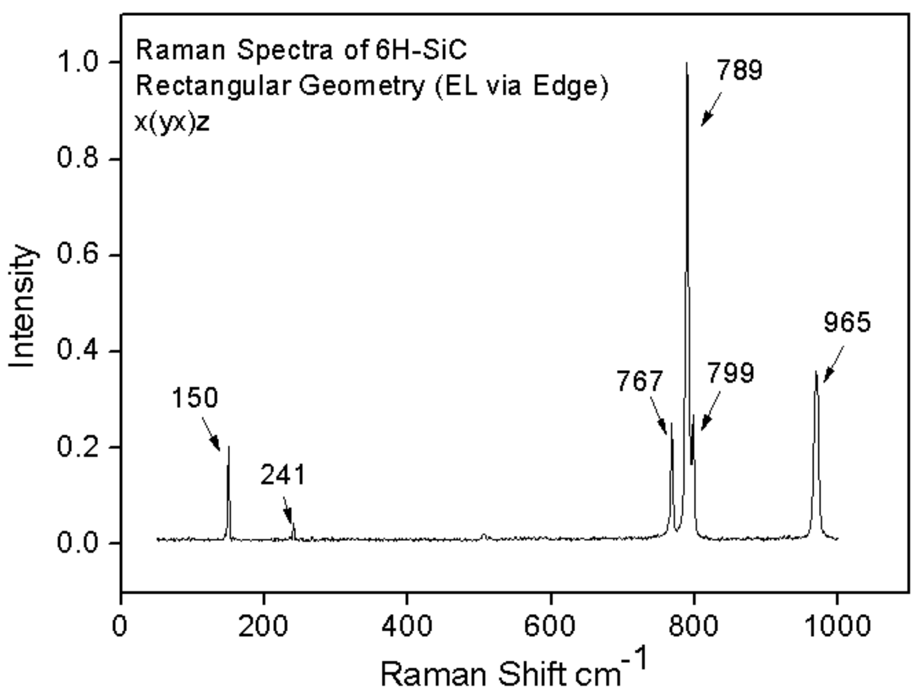

(b)

Fig.4.19. Raman Spectra of 4H-SiC for Rectangular geometry (excited via Edge), where a) represents $x(zy)z$ configuration and b) represents $x(yx)z$ configuration.

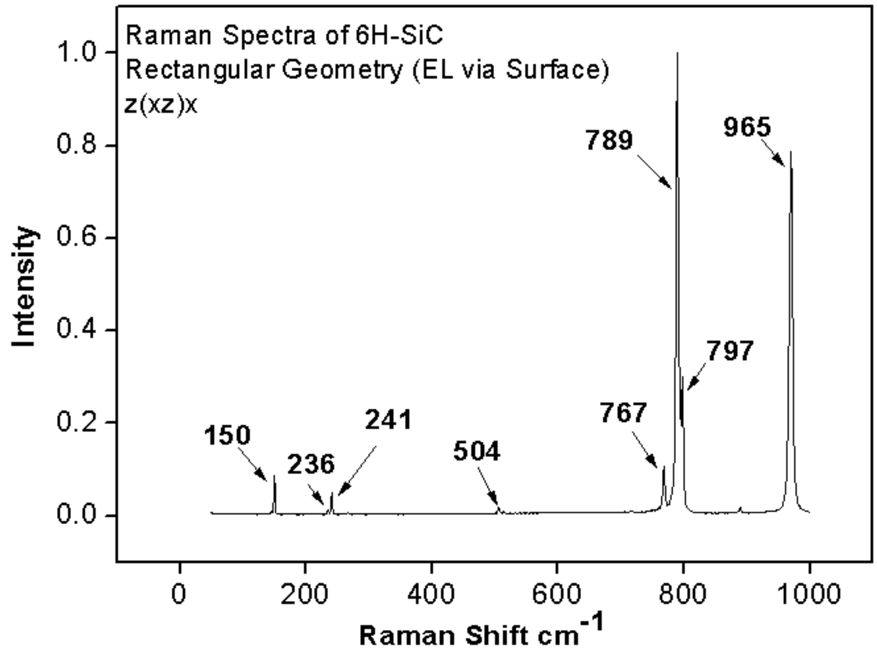

(a)

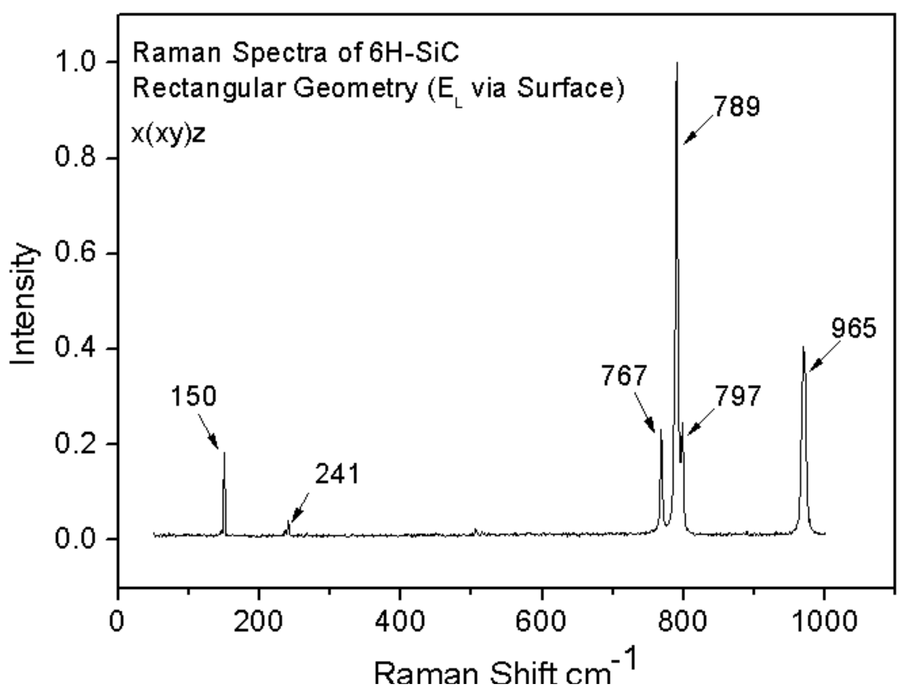

(b)

Fig.4.20. Raman Spectra of 4H-SiC for Rectangular geometry (excited via Surface), where a) represents $z(xz)x$ configuration and b) represents $z(xy)x$ configuration.

5. Conclusions

The purpose of this study was to explore the possibilities for extracting maximum information about the phonon properties of 4H, 6H and possibly, higher polytypes of SiC from the Raman Spectra recorded in different geometries, as well as from the infrared reflection and transmission spectra. We have shown that observation of spectra recorded in different geometries is crucial for the assignment of phonons symmetries to the experimentally observed lines. Raman spectroscopy offers more flexibility than the IR spectroscopy in this respect without special sample preparation. In addition, Raman spectroscopy allows studying phonons with energies within the IR Restrahlen band and is, therefore, preferable technique.

Aided by the lattice dynamical model (LDM) and group theoretical considerations, we have been able to assign symmetries to the phonons associated with different lines in the Raman spectra. However, in some cases this assignment should be treated as tentative, because the existing theory does not explains completely the all intensity variations of the lines with the experimental geometry. We believe that adequate description may be obtained if the macroscopic model for the susceptibility of the crystal is built, and we are now in process of development of such a model using the so-called bond polarizability concept.

A rigorous identification of the mode symmetries will provide important feed back information to lattice dynamic calculation. So far, such calculations employ information about the phonon energies and not about associated symmetries. As a consequence, usually the LDM provides good description of the phonons energies, where as this is well known within this field that the eigenvectors (i.e., the corresponding atomic displacements as calculated by theory) are quite wrong employing experimentally-found symmetries in conjunction with the corresponding phonon energies will certainly provide a ground for improvement for LDM.

Finally, we have found empirically (using our LDM) that the ionicity of the bonding is the major (if not the only) parameter of affecting the shift of LO mode and splitting of the TO modes with changing the direction of the phonon wave vector with respect to the crystal axis. Since this shift and splitting can be easily measured using different Raman arrangements, the experiment provides a measure for the ionicity of the crystal. In the case of 4H-SiC, we find that the experimentally observed splitting and shift are very well reproduced by our LDM if ionicity of 12% is used, a value in excellent agreement with the literature data [29].

5.1. Future Directions

The perspective for future work is to build full microscopic model of polarizability of lattice based on the so-called Bond-Polarizability Model. That will provide more incite into our experimental result. From this model we can construct explicit expressions for the component of polarizability derivative and we can even expect to be able to be synthesize the whole spectrum theoretically. The main goal of this diploma work was to obtain the experimental data and provide initial identification of the lines, which will be used for rather more detailed comparison with theory in future.

References

1. Carl Hemmingsson, Deep levels in electron-irradiated and as grown SiC power device materials, Dissertation thesis, Material Science Dept, Linköping University, Sweden, 1998.
2. Tairov, Tsvetkov, Journal of crystal growth 43 (1978) 209-212.
3. Marko Tuominen, Growth and structural characterization of SiC crystal, dissertation thesis, Material Science Dept, Linköping University, Sweden, 1997.
4. http://www.ifm.liu.se/matephys/news/SiC.
5. Jie Zhang, CVD growth and Material quality control of SiC, Dissertation thesis, Material Science Dept, Linköping University, Sweden, 2001.
6. Mark Fox, Optical properties of Solids, 1st Edition, 2001.
7. Peter Bruesch, Phonons Theory and Experiments I, Vol #34, 1982.
8. C.Kittel, Introduction to solid State Physics, 7th Edition.
9. H. Kuzmany, Solid State Spectroscopy-An Introduction, Peter Bruesch, Phonons: Theory and Experiments II.
10. Online Journal of Vibrational Spectroscopy, http://www.ijvs.com/archive.html
11. Jon Matthews and R.l. Walker, Mathematical Methods of physics, 2nd Edition, 1969.
12. Hayes and Loudon, Scattering of light by crystals, 1978.
13. Group theory and quantum mechanics,Tinkum, 1964
14. Group Theory in Physics I & II, J.F.Cornwell
15. S.Nakashima, and H.Harima, Raman Investigation of SiC Polytypes, phys. stat. sol. 1997.
16. D.W.Feldman, James.H.Parker, W.J.Choyke and Lyle Patrick, Raman Scattering in 6H-SiC, Westinghouse Research Laboratories, Pittsburgh, Pennsylvania, 1967.
17. Phonon replicas at the M point in 4H-SiC: A theoretical and experimental study, I.G.Ivanov, Lindefelt, A.Henry, O.Kordina.
18. D.S.Balchuk, N.M.Beliy, V.P. Gubanov, V.A. Gubanov, V.K. Kononov, Symmetry of vibrational modes, Invariance of energy states under time inversion and Raman scattering in 4H and 6H-SiC, Ukrainskij Fiziceskij Zurnal, vol.41 (2), p.146, 1996 (in Ukrainian).
19. J.Tersoff, Phys.Rev.B 39, 5566, 1989
20. C.Q.Chen, R.Helbig, F.Engelbrecht, Infrared absorption spectra of 4H-SiC, Applied Physics A, August 2000.
21. W.G.Spitzer, D.Kleinman, Infrared Properties of Hexagonal Silicon Carbide, Physical Review, Vol 113, Number 1, 1959.
22. D.W.Feldman, James.H.Parker, Phonon Dispersion Curves by Raman Scattering in SiC, Physical Review, Vol 173, Number 1, 1968.
23. M.F.McMillan, R.P.Devaty, Interference Fringes in the Infrared Reflectance of 6H-SiC substrates, University of Pittsburgh, USA
24. Lyle Patrick and W.J.Choyke, Lattice Bands in SiC, Physical Review, Vol 123, Number 3, 1961.
25. M.Hoffman, A. Zywietz, K.Karch, Lattice Dynamics of SiC polytypes within the Bond Charge Model, Physical Review B, vol 50, Number 18, 1994.
26. G.P.Srivastava, The Physics of Phonons
27. http://www.mpip-mainz.mpg.de.html
28. Project report on Fundamental and Summation Lattice Band Analysis in 4H and 6H - SiC by Infrared Spectroscopy, Hina Ashraf, Ivan Ivanov, Björn Magnusson and Erik Janzén, Department of Physics and Measurement Technology, Linköping University, SE-581 83 Linköping, Sweden

29. Investigation of Symmetries of Phonons in 4H and 6H-SiC by Infrared Absorption and Raman Spectroscopy, Hina Ashraf, Ivan Ivanov.
30. A.A. Maradudin, Group-theoretic analysis of long-wavelength vibrations of polar crystals, Dept of Physics, University of California, 1975.
31. S.Nakashima, K.Tahara, Wave-vector dependence of Raman scattering intensity in folded modes of long period α- SiC, Osaka University, 1989.
32. J.C.Burton and L.Sun, Department of chemistry, Rutgers University, First and second-order Raman scattering from semi insulating 4H-SiC, 1998.
33. S.Nakashima, Yashuro Nkakura, Structural identification of SiC polytypes by Raman scattering: 27R and33R polytypes, Osaka university, Journal of the physical society of Japan, Vol.56, No. 1,1987.
34. S. Nakashima, H.Katahama, Relative Raman intensity of the folded modes in SiC polytypes, Dept of applied physics, Osaka University, Phys Rev B, 1985.
35. C.H.Hodges, Theory of phonon dispersion curves in SiC polytypes, Phys Rev, 1969.
36. R.p.Devaty and W.J.Choyke, Optical characterization of Silicon Carbide, Dept of physics, University of Pittsburgh, phys.stat.sol. (a) 162, 5 (1997).
37. W.J.Choyke, Optical and electronic properties of SiC, Dept of physics, University of Pittsburgh.